WestVirginiaUniversity
THE RESEARCH REPOSITORY @ WVU

Faculty Scholarship

2013

Radio Continuum Observations Of Local Star-Forming Galaxies Using The Caltech Continuum Backend On The Green Bank Telescope

Katie Rabidoux

D. J. Pisano

Amanda A. Kepley

Kelsey E. Johnson

Dana S. Balser

Follow this and additional works at: https://researchrepository.wvu.edu/faculty_publications

Radio continuum observations of local star-forming galaxies using the Caltech Continuum Backend on the Green Bank Telescope

Katie Rabidoux, D.J. Pisano[1]

Department of Physics and Astronomy, West Virginia University, 135 Willey St., P.O. Box 6315 Morgantown, WV 26506

Amanda A. Kepley[2,3], Kelsey E. Johnson[4]

Department of Astronomy, University of Virginia, P.O. Box 400325, Charlottesville, VA 22904

and

Dana S. Balser

National Radio Astronomy Observatory, 520 Edgemont Road, Charlottesville, VA 22904

ABSTRACT

We observed radio continuum emission in 27 local (D < 70 Mpc) star-forming galaxies with the Robert C. Byrd Green Bank Telescope between 26 GHz and 40 GHz using the Caltech Continuum Backend. We obtained detections for 22 of these galaxies at all four sub-bands and four more marginal detections by taking the average flux across the entire bandwidth. This is the first detection (full or marginal) at these frequencies for 22 of these galaxies. We fit spectral energy distributions (SEDs) for all of the four-sub-band detections. For 14 of the galaxies, SEDs were best fit by a combination of thermal free-free and nonthermal synchrotron components. Eight galaxies with four-sub-band detections had steep spectra that were only fit by a single nonthermal component. Using these fits, we calculated supernova rates, total number of equivalent O stars, and star formation rates within each $\sim 23''$ beam. For unresolved galaxies, these physical properties characterize the galaxies' recent star formation on a global scale. We confirm that the radio-far-infrared correlation holds for the unresolved galaxies' total 33 GHz flux regardless of their thermal fractions, though the scatter on this correlation is larger

---

[1]Adjunct Assistant Astronomer at National Radio Astronomy Observatory, P.O. Box 2, Rt. 28/92, Green Bank, WV 24944

[2]Current address: National Radio Astronomy Observatory, P.O. Box 2, Rt. 28/92, Green Bank, WV 24944

[3]Visiting Research Associate at National Radio Astronomy Observatory, 520 Edgemont Road, Charlottesville, VA 22904

[4]Adjunct Assistant Astronomer at National Radio Astronomy Observatory, 520 Edgemont Road, Charlottesville, VA 22904

than that at 1.4 GHz. In addition, we found that for the unresolved galaxies, there is an inverse relationship between the ratio of 33 GHz flux to total far-infrared flux and the steepness of the galaxy's spectral index between 1.4 GHz and 33 GHz. This relationship could be an indicator of the timescale of the observed episode of star formation.

Subject headings: galaxies: star formation — radio continuum: galaxies

1. Introduction

Radio continuum emission traces star formation on timescales of up to 100 Myr (Condon 1992). Two physical processes resulting from massive star formation produce most of the radio continuum emission between 1 and 100 GHz in star-forming galaxies: (1) nonthermal synchrotron emission from relativistic electrons accelerated by magnetic fields as a result of recent supernovae and (2) thermal free-free emission from gas ionized by young massive stars (Condon 1992). The nonthermal emission is closely tied to the number of supernova-generating massive stars produced in recent episodes of star formation, while the thermal emission gives a nearly direct measure of the current equivalent number of O stars via the ionizing flux in the sampled area. Since each component traces a physical process with a well-known timescale, we can use measurements of the radio continuum to determine star formation rates and constrain the ages of recent episodes of star formation.

Recent studies of nearby star-forming galaxies with interferometers have emphasized resolving individual star-forming regions (e.g. Beck, Turner, and Kovo 2000; Johnson, Indebetouw, and Pisano 2003; Johnson and Kobulnicky 2003; Johnson et al. 2004; Tsai et al. 2006; Reines, Johnson, and Goss 2008; Johnson, Hunt, and Reines 2009; Aversa et al. 2011). Since radio continuum emission is not affected by extinction, it can be used to observe deeply embedded regions of current star formation that have not yet shed their surrounding material and are thus invisible at shorter wavelengths. These studies have taken advantage of interferometers' exceptional spatial resolution to probe very young starbursts whose optical emission is obscured by dust. While these studies have been invaluable for determining star formation properties in galaxies outside of our own, the high angular resolution and missing short-spacing data of interferometers, especially at higher frequencies, "resolves out" the diffuse radio continuum emission outside of compact star-forming regions. This effect disproportionally impacts synchrotron emission, which tends to be much more diffuse than the primarily thermal emission surrounding areas of ongoing massive star formation (Johnson et al. 2009). Unlike interferometers, single dish telescopes are not plagued by missing short spacings. Therefore, these telescopes provide a way to simultaneously measure the compact thermal and diffuse nonthermal components of a galaxy's radio continuum emission in order to characterize its *global* star formation properties.

Determining the relative contributions of the thermal and nonthermal components of the measured flux of entire galaxies can be challenging. Fortunately, each component has a distinct behavior

with respect to frequency, and therefore we can model radio continuum emission with a simple two-component fit. Radio continuum flux follows a power law relation such that $S_\nu \propto \nu^\alpha$, where α is the spectral index that is characteristic of a source's emission. Optically thin thermal emission exhibits $\alpha = $ -0.1, and nonthermal emission exhibits $\alpha \approx $ -0.8 (Condon 1992). To determine a reliable fit to these parameters, observations sampling the same physical area at multiple, widely-spaced frequencies are required. If only one frequency is observed, it is impossible to determine the relative contributions of each emission process without previous knowledge of the source. Since single dish telescopes are sensitive to both compact thermal and diffuse nonthermal emission over large spatial extents, they are useful for constraining the large-scale properties of multiple components of a galaxy's radio continuum emission, and are thus powerful probes of star formation.

The goal of this paper is to characterize the *global* star formation properties of local galaxies. Our observations were taken in four independent channels continuous in frequency across the full 26-40 GHz span of Ka band. This range in frequencies is where a typical star-forming galaxy's global radio continuum emission would be expected to contain relatively equal amounts of flux from steep-spectrum synchrotron and flat-spectrum thermal sources (Condon 1992). Our observations are thus ideal for approximating the relative contributions of each type of emission at this "lever arm" frequency range. Using new radio continuum observations centered at 27.75 GHz, 31.25 GHz, 34.75 GHz, and 38.25 GHz, as well as archival NVSS 1.4 GHz and IRAS 60 μm and 100 μm data, we have determined these galaxies' thermal fractions and star formation rates. We have also explored the radio-far-infrared correlation in these galaxies and its implications for their star formation timescales. We will describe the galaxy sample and our observations and data reduction in Section 2, present our results and address the process of fitting spectral energy distributions to our data in Section 3, and finally conclude in Section 4.

2. Data

2.1. Sample Selection

We selected a heterogeneous group of 27 local (D < 70 Mpc), well-studied star-forming galaxies with known thermal radio continuum emission. Our sample contains galaxies spanning a variety of shapes, sizes, and environments, from blue compact dwarfs to grand-design spirals, including major and minor mergers, with members of compact groups as well as more isolated galaxies (see Table 1 for galaxy types). The intention was to observe as many types of star-forming galaxies as possible to probe star formation in a diverse range of environments. See Table 1 and Figure 1 for sample properties. For more information on each galaxy's previous radio continuum observations and discussions of their properties, see the papers named in Table 1.

The galaxies in our sample span a range of distances (1-70 Mpc) and properties. They all have previously detected radio emission and ongoing star formation that covers three orders of magnitude in star formation rate. Thus, they are strong targets for a study of global radio continuum properties

at a frequency range that probes both thermal free-free and nonthermal synchrotron star formation indicators. As seen in Figure 1, these galaxies are largely less massive and have higher star formation rates than the Milky Way, and have subsolar metallicities. However, their properties are not so similar that they can be considered as a single class. It would not be surprising if their radio continuum properties also encompassed a range of values. Our analysis is best understood as reflecting properties of nearby star-forming galaxies, though it is beyond the scope of this paper to perform detailed analysis on each galaxy individually.

2.2. Observations and Data Reduction

We observed the galaxies in our sample with the Caltech Continuum Backend (CCB) on the Robert C. Byrd Green Bank Telescope (GBT)[5] using single pointings. The CCB is designed for the GBT's dual-beam Ka band receiver spanning the entire range of frequencies from 26-40 GHz. The primary observing mode of the CCB is a 70 second "nod", where each beam takes a turn as the on-source beam while the other beam is off-source. We observed 24 of the galaxies using a single nod each, while we observed eight galaxies using multiple nods, which we then averaged. Five galaxies in our sample were observed on two different nights with both of these methods; we treated these on a case-by-case basis and chose the observation(s) with the best weather and elevation conditions. We used the standard NRAO primary flux calibrators 3C 147 and 3C 48 for flux calibration, as well as nearby pointing calibrators to ensure accurate pointing. See Table 1 for a summary of the observations.

We reduced our data using IDL reduction routines developed by B. Mason (for details on the data reduction process, see Mason et al. 2009). Data with wind speeds over 5 m s^{-1} were excluded due to the possibility of large pointing errors. We detected 22 galaxies in all four channels. When a galaxy's flux was lower than the 2σ level in one or more of the four channels, we combined the channels' fluxes to produce one average flux across the entire band, centered at 33 GHz. One galaxy, Pox 4, was detected at the 5σ level after averaging the four channels. Three additional galaxies were marginally detected (between 2σ and 3σ) using this method. We report an upper limit 33 GHz flux for one galaxy, Tol 35. The galaxies' observed fluxes are reported in Table 2.

Since the angular size of a telescope's beam is inversely proportional to the frequency observed, the beam size of the GBT varies appreciably across the 26-40 GHz range of our observations ($\sim 27''$ in the lowest-frequency sub-band versus $\sim 19''$ in the highest-frequency sub-band, see Figure 2 for an illustration). We followed the procedure of Murphy et al. (2010) to correct for differing beam sizes in each of the four sub-bands. First, we imaged an archival VLA radio continuum map of each galaxy (typically at frequencies of 4-10 GHz) using the AIPS task IMAGR. For these maps, we

---

[5]The National Radio Astronomy Observatory is a facility of the National Science Foundation operated under cooperative agreement by Associated Universities, Inc.

selected the archival UV data from the NRAO science data archive[6] with the closest beamsize to our Ka-band data. We explicitly imposed each of the four CCB beam sizes on these images using BMIN and BMAJ (assuming a circular beam). We determined correction factors for each beam by normalizing the flux contained in each beam area in the archival map to the flux in the 34.75 GHz port's $\sim 21''$ beam. This procedure partially adjusts for more flux being observed at lower frequencies due to these frequencies' intrinsically larger beam sizes. We then could approximate "beam-matched" flux measurements to determine spectral indices between 26-40 GHz (see Figure 3 for an illustration of the galaxies' spectral indices before and after applying the corrections). NGC 1222 did not have available archival data, so we applied to it the average correction factors of all of the other galaxies. We emphasize that these correction factors are only approximate. In many cases, they are based on resolved archival images that may not contain all of the galaxies' radio flux. In particular, these resolved images may contain most of the thermal emission, which tends to be compact, but underestimate the galaxies' nonthermal emission, which tends to be diffuse. This could bias the correction factors to be closer to 1.0 than should be the case, especially in the highest-frequency (and thus highest-resolution) channel. See Table 3 for the beam correction factors for each galaxy.

The dominant sources of uncertainty in our beam corrections are systematic errors due to the geometries of our sources. The smallest corrections possible are for a galaxy whose most diffuse, extended flux is still contained within the smallest beam and is unresolved by the lower-frequency interferometric observations. This type of source would look identical to all four of the GBT beam sizes. In this case, the correction factors would be 1.0 for each sub-band. For a source much more extended than the beam sizes, the maximum deviations from no beam corrections in each sub-band are -36%, -19%, 0%, and +21%. Pointing offsets from the peak of radio emission can also be sources of systematic error, though the errors depend on whether the source is compact or extended, and the magnitude of the pointing offset from the central peak of radio emission. These errors are typically smaller than the maximum deviations discussed above. Since we do not know how much diffuse emission is missing in the archival data, we do not have enough information to quantify uncertainties in the beam correction factors for each galaxy.

Many of the galaxies that we observed were more extended than the $\sim 23''$ beam size of the GBT at 33 GHz. In these cases, radio continuum fluxes and star formation rates should only be interpreted as covering the inner $\sim 23''$ of the galaxies. The galaxies with resolved lower-frequency archival data that was more extended than the beam size are flagged with a "1" in Table 4.

The CCB has a beam separation of $78''$ between the "on" and "off" beams. M 51 and M 101 are more extended than that separation in both optical images (see Figure 4) and in maps of their lower-frequency radio continuum emission (Klein et al. 1984; Graeve et al. 1990). In these cases, our flux measurements may be lower than the true amount of flux contained within the beam. There is likely to be radio continuum emission at the "off" positions, which would cause an

---

[6]https://archive.nrao.edu

oversubtraction of flux in the reduction process.

3.   Results and Discussion

3.1.   Fluxes

For 22 of the 27 galaxies that we observed, the fluxes we report are the first detections (either in all four sub-bands or averaged) at $\sim$33 GHz. Four of the galaxies in our sample were previously observed with the CCB by Murphy et al. (2012), three of which were detected (M 101 was reported as an upper limit by Murphy et al. (2012) and is a 2.6σ marginal detection when the four sub-bands were averaged in our observations). Only one galaxy in our sample, Tol 35, was not detected when averaging four sub-bands' fluxes. Its 3σ upper-limit flux is 0.87 mJy. This galaxy was observed at a very low elevation (7.9°), so it was observed with large atmospheric extinction. See Table 2 for the uncorrected fluxes, and Table 4 for the fluxes corrected for the differing beam sizes of each frequency.

3.2.   Spectral energy distribution fitting

We fit a spectral energy distribution (SED) for each galaxy that was detected in all four sub-bands using the four CCB fluxes and archival NRAO VLA Sky Survey (NVSS) 1.4 GHz fluxes (measured with a 45″ aperture). We assumed a two-component fit of nonthermal emission with a spectral index α_N = -0.8 and thermal emission with a spectral index α_T = -0.1. These fits are plotted in Figure 5. Though the spectral index of nonthermal emission can vary (this phenomenon is described further in Section 3.2.1), we used this simple model because we only fit to five data points for each galaxy; our model did not include enough data to justify additional free parameters. We do not see evidence of anomalous dust emission in the observed regions of these galaxies (for explanations of anomalous dust, see Draine & Lazarian 1998; Murphy et al. 2010). Our observations are also at frequencies low enough to have negligible contributions from the low-frequency tail of the dust blackbody. Therefore, we did not include any thermal dust emission in our fits. Our spectra also do not show the inverted structure characteristic of self-absorption or optically thick thermal emission, so we did not include either of these components. From these fits, we determined each galaxy's thermal and nonthermal fluxes at 33 GHz.

None of the galaxies have globally flat spectra indicative of purely thermal emission, nor the inverted spectra seen in some resolved observations of very young, obscured thermal sources. Thermal emission was the primary component at 33 GHz in some galaxies, while others had less prominent or even negligible thermal components in the observed regions. In contrast to radio continuum studies done at high spatial resolution, our single dish observations detect the diffuse synchrotron emission produced by past supernovae in addition to the strong compact thermal emission from

H II regions, so the spectral indices that we derive are typically much steeper than those derived only from detections of compact radio sources. Since our observations do not spatially separate regions of thermal and nonthermal emission, we cannot further distinguish the two components in that way.

3.2.1. Galaxies with steep radio spectra

The fitted spectra for eight of the 27 galaxies (Arp 217, NGC 4449, NGC 2903, Maffei II, NGC 4038, M 51, NGC 4490, and NGC 1741) are significantly steeper than can be fit by a combination of thermal (α_T = -0.1) and nonthermal (α_N = -0.8) components (see Figure 5). When we could not fit a galaxy's SED with both the thermal and nonthermal components at the 2σ level, we used only a single-component fit that assumed no thermal flux and a fixed nonthermal spectral index of α_N = -0.8 for consistency. The thermal fluxes and associated properties of this group of galaxies are reported as upper limits. We used the total flux in the 34.75 GHz channel plus 3σ as a conservative upper limit to the thermal flux in these cases.

There are two possible explanations for the steep spectra that we see in some galaxies. There could be technical considerations due to imperfect beam-matching in our data, or there could be physical processes taking place within these galaxies causing their spectra to steepen at high frequencies. In order to have more accurate SED fits—and more precise star formation rates—we would need to have beam-matched observations of the same regions at many different frequencies.

The correction factors for differing beam sizes that are given in Table 3 are limited by being calculated using higher-resolution data that could be missing extended emission. If extended emission is missing in the archival data, the correction factors in Table 3 could be closer to 1.0 than is actually the case. While all of the correction factors calculated act to flatten the SED between 26 GHz and 40 GHz with respect to the uncorrected data, it is possible that they do not flatten the SED enough if they do not reflect contributions from extended emission (as discussed in Section 2.2). In addition, we did not correct for mismatched beams between the $\sim 45''$ NVSS data and the $\sim 23''$ CCB data. This beam difference only affects resolved galaxies (those marked with a "1" in Table 4), which comprise 33% of our sample. It is possible that synchrotron emission is more adversely affected by the differences in beam sizes than thermal emission. More diffuse synchrotron emission could be undetected at higher frequencies (and thus smaller beam sizes) than would be expected for a smooth flux distribution observed with two apertures of different sizes. If this is the case in our observed regions, it could explain why some of our galaxies' spectra steepen at the frequencies we observed. It is also possible that the choice of where the GBT beams were pointed within a galaxy could affect its fluxes in different beam sizes. If the beam is not centered on the galaxy (in the case of unresolved galaxies) or is not centered on a bright knot of emission (in the case of resolved galaxies), the smaller beams could contain even less flux than would be expected after corretions for the beams' areas. NGC 1741 and NGC 4490 are likely affected by pointing offsets, as seen by comparing the GBT pointing in Table 1 to previous radio continuum

maps in Figure 2 of Beck et al. (2000) and Figure 4 of Aversa et al. (2011). As described in Section 2.2, pointing offsets from the peak of radio continuum emission result in the need for larger beam correction factors than derived from the archival radio continuum data, the lack of which result in steep spectra at the observed frequencies.

In addition to the technical issue of mismatched beam sizes, there are possible physical explanations for steep spectra in star-forming galaxies. It is difficult to distinguish between a spectrum with a nonthermal component having $\alpha_N \approx -0.8$ coupled with a low thermal fraction from a spectrum with a steeper nonthermal component coupled with a relatively high thermal fraction (Condon 1992). Though the spectral indices that we used are typical values (Condon 1992), they can vary depending on the physical parameters of the observed regions. Thermal emission can have a positive spectral index if the emission regions are optically thick, though we do not see any evidence that this is occuring on the angular scale of our observations. Nonthermal spectral indices can be positive at low frequencies due to synchrotron self-absorption (which we do not observe), or become more negative with increasing frequency and increasing scale height from the disk due to aging cosmic ray electrons losing energy as they propagate outward from their parent supernovae (Seaquist et al. 1985; Carlstrom & Kronberg 1991; Heesen et al. 2009). Kepley et al. (2011) calculated the timescale for synchrotron losses for cosmic ray electrons in NGC 4214 to be 44 Myr at 1.4 GHz and 18 Myr at 8.5 GHz. There is also some evidence of steepening spectra at higher frequencies ($\gtrsim$ 10 GHz) for luminous and ultra-luminous infrared galaxies, as well as in the post-starburst galaxy NGC 1569 (Israel & de Bruyn 1988; Lisenfeld et al. 2004; Clemens et al. 2008, 2010; Leroy et al. 2011). These authors hypothesize that winds or outflows may disperse synchrotron emission from its parent source more quickly than would be expected for simple diffusion. This rapid dispersal could cause a dearth of synchrotron emission at higher frequencies on shorter timescales than would be predicted from the timescale of energy loss. Leroy et al. (2011) also hypothesize that there could be a modified injection spectrum in galaxies where this is the case. Our sample of galaxies does not contain any LIRGs or ULIRGs, and we do not see steepening in our measurements of NGC 1569. We are only observing the inner region of NGC 1569, while the dispersed synchrotron emission resides in its outer halo, so it is not surprising that we do not observe a steepening spectrum in this galaxy.

We suspect that the steep spectra seen in our sample are primarily a result of imperfect beam matching as discussed above. This is especially likely to be the case for the galaxies resolved by the GBT at 33 GHz, since these galaxies will have emission that is outside of the view of the GBT beam but is included in the NVSS flux. As discussed earlier, the galaxies that appear unresolved in archival maps could still have diffuse synchrotron emission that was not detected in the archival data but that is more extended than the $23''$ beam at 33 GHz. Five of the eight resolved galaxies that were detected in all sub-bands had steep spectra (four out of those five are classified as spiral galaxies), while only three of the fourteen unresolved galaxies had this feature. Two of these three are classified as SABbc galaxies, while the third is classified as peculiar. It is possible that these steep-spectrum galaxies contain emission in their spiral arms that is extended with respect

to the GBT's smaller beam but is observed in the NVSS data. In Figure 5, most of the galaxies with steep spectra (and thus single component fits) also showed the NVSS 1.4 GHz data point being located above the best-fit line expected for purely nonthermal emission. This could be a consequence of the larger beam at 1.4 GHz sampling a larger physical area of emission. Even so, the alternative physical explanations merit consideration, especially in the case of the unresolved galaxies. In Figure 7, which will be discussed further in Section 4.6, the three unresolved galaxies with steep spectra (NGC 1741, NGC 2903, and Arp 217) have elevated 1.4 GHz fluxes with respect to what would be expected from the radio-far infrared correlation. Since the 33 GHz fluxes of these galaxies are not similarly elevated with respect to their far-infrared fluxes in Figure 7, their steep radio spectra may indicate an internal physical process that strongly increases the amount of synchrotron emission.

3.3. Thermal fractions

The average thermal fraction fit by two-component models at 33 GHz was 54%, with a 1σ scatter of 24% and a range of 10%-90%. The average is consistent, albeit with large scatter, with the average global thermal fraction at 33 GHz in star-forming galaxies without active galactic nuclei following the relation

$$\frac{S}{S_T} \sim 1 + 10 \left(\frac{\nu}{GHz}\right)^{0.1+\alpha_N} \tag{1}$$

where $\alpha_N = -0.8$ is the nonthermal spectral index, S_T is the thermal flux at a given frequency, and S is the total flux at that frequency (Condon & Yin 1990). When a two-component fit was not possible, we report the thermal flux as the corrected flux at 34.75 GHz plus 3σ, which gives a very conservative upper limit. We expect from the galaxies' SEDs that their true thermal fractions are very low at 33 GHz, which we assume in the rest of our analysis.

3.3.1. Implications for star formation timescales

The large scatter in the thermal fraction is likely a consequence of our heterogeneous galaxy sample; these galaxies are at different stages of evolution and have different star formation rates, stellar populations, and physical properties (Beck et al. 2000). Some of them may have a very recent (< 10 Myr) burst of star formation that produces a large amount of free-free emission that dominates their spectra from 1-100 GHz. Others may be in between episodes of very active star formation and instead be experiencing a more quiescent phase, which would result in a relatively low thermal fraction and steepening nonthermal component at 33 GHz due to synchrotron energy losses at high frequencies.

Thermal emission traces very recent star formation, since it comes from ionized regions around short-lived, massive stars. For a single starburst, a spectrum showing solely thermal emission requires that too few supernovae have yet occurred to detect their emission. This would constrain

the starburst to be less than ~ 6 Myr old (or even younger, depending on the mass and lifetime of the most massive O stars in the starburst; Maeder & Meynet (1989) find the lifetime of a 120 $M_{\odot}$ star to be 3.4 Myr). A complete absence of thermal flux implies the absence of enough massive O stars to have detectable free-free emission for a long enough period of time that the emission has dissipated from its parent region. If this was the case, the starburst is likely at least 30 Myr old (the lifetime of the least massive supernova progenitors). On the other hand, nonthermal emission probes star formation on longer timescales (30 Myr $< \tau < 100$ Myr). It is produced by recent supernovae of stars that can be less massive and have longer lifetimes than the O stars that produce thermal emission (see Figure 9 of Condon 1992). The presence of nonthermal emission implies that the starburst is at least 6 Myr old but younger than the timescale dictated by synchrotron energy loss for the galaxy's magnetic field (~ 100 Myr) (Condon 1992).

We note that there are limits to the amount of each component that we can detect, so the timescales quoted in the previous paragraph are only approximate. To constrain how much nonthermal emission could be present in a spectrum that appears purely thermal, we generated spectra with varying thermal fractions with fluxes at the same five frequencies as those in our data set (1.4 GHz, 27.75 GHz, 31.25 GHz, 34.75 GHz, and 38.25 GHz) and 10% errors on the fluxes. When these spectra are fit with a two-component model assuming $\alpha_T = -0.1$ and $\alpha_N = -0.8$, nonthermal emission can only be detected in the spectra for thermal fractions less than 97%. This means that the galaxy could have some nonthermal emission (up to 3% for 10% errors on the fluxes), but the emission would be undetectable and thus the starburst would appear younger than it is. Similarly, a spectrum could look like it contains no thermal emission while actually containing quite a bit. For the same spectra with 10% errors on the fluxes, thermal fractions of up to 20% resulted in undetectable thermal components. This means that a galaxy could look like its massive star formation has ceased while still having a small thermal component.

For the galaxies in our sample, this picture could be more complicated. The quoted timescales in this section are for an isolated single starburst. Since our observations measure star formation properties on large angular scales, the galaxies may have multiple overlapping generations of star formation that are not easily separated in time. We are also sampling different structures and physical scales in each galaxy. For some galaxies, we are only observing the most central region. For these galaxies, we may be missing the majority of the ongoing star formation happening in outer regions and spiral arms. For the more compact galaxies, however, we are likely measuring the entirety of the galaxy's star formation within the GBT beam, so our measurements characterize their global star formation properties.

3.4. O stars producing ionizing photons

For those galaxies whose SEDs were fit with thermal components, we used their fluxes at 33 GHz to calculate their thermal luminosities. We then used those luminosities to calculate the number of ionizing photons responsible for the thermal fluxes seen within the GBT beam following

Equation 2 in Condon (1992):

$$\left(\frac{Q_{Lyc}}{s^{-1}}\right) \geq 6.3 \times 10^{52} \left(\frac{T_e}{10^4 K}\right)^{-0.45} \left(\frac{\nu}{GHz}\right)^{0.1} \left(\frac{L_T}{10^{20} W H z^{-1}}\right), \tag{2}$$

where Q_{Lyc} is the number of Lyman continuum photons emitted by the region on thermal emission, T_e is the electron temperature, and L_T is the thermal luminosity. The resulting values are detailed in Table 5 (unresolved galaxies) and Table 6 (resolved galaxies). We used an electron temperature of 10^4K, as is typical for star-forming regions (Condon 1992), and used $Q_0 = 10^{49} s^{-1}$ as the number of Lyman continuum photons emitted by an O7.5V star from Table 5 in Vacca et al. (1996). We report the total number of O7.5V stars in the galaxies that are unresolved by the GBT at 33 GHz, and the number of O7.5V stars per square kiloparsec for the resolved galaxies in Tables 5 and 6. As seen in Table 5, the number of O7.5V stars in each unresolved galaxy varies widely (log # O7.5V stars is between 2.42 and 4.66). This is likely due to the wide range in the unresolved galaxies' overall star formation rates and physical areas observed.

3.5. Supernova rates

Since we were able to fit nonthermal components for all of our galaxies, we calculated supernova rates (ν_{SN}) for each of them following Equation 18 in Condon (1992):

$$\left(\frac{L_N}{10^{22} W H z^{-1}}\right) \sim 13 \left(\frac{\nu}{GHz}\right)^{-0.8} \left(\frac{\nu_{SN}}{yr^{-1}}\right), \tag{3}$$

where L_N is the nonthermal luminosity. We report the total supernova rate of the unresolved galaxies in Table 5, while for the resolved galaxies we report the supernova rate per square kiloparsec in Table 6. The supernova rates of the unresolved galaxies vary by three orders of magnitude (log SNe rate between -3.72 and -0.71), which is not surprising given the differences in star formation rates and physical areas sampled.

3.6. Star formation rates

We calculated massive star formation rates (SFRs) from thermal fluxes for each galaxy whose SEDs have a thermal component and from nonthermal fluxes for all of our galaxies following Equations 21 and 23 of Condon (1992):

$$\left(\frac{L_N}{W H z^{-1}}\right) \sim 5.3 \times 10^{21} \left(\frac{\nu}{GHz}\right)^{-0.8} \left(\frac{SFR_N\,(M \geq 5M_\odot)}{M_\odot yr^{-1}}\right) \tag{4}$$

$$\left(\frac{L_T}{W H z^{-1}}\right) \sim 5.5 \times 10^{20} \left(\frac{\nu}{GHz}\right)^{-0.1} \left(\frac{SFR_T\,(M \geq 5M_\odot)}{M_\odot yr^{-1}}\right) \tag{5}$$

where L_T and L_N are thermal and nonthermal luminosities, respectively, calculated from each galaxy's thermal and nonthermal fluxes, and $\nu = 33$ GHz. These equations are derived from

Equations 2 and 18 of Condon (1992) (reproduced as Equations 2 and 3 in this paper). Those equations were derived assuming (1) an extended Miller-Scalo IMF (Miller & Scalo 1979) with an exponent of -2.5, (2) that all stars with masses greater than $8M_\odot$ become supernovae, and (3) that dust absorption is negligible (Condon 1992). We then scaled the massive SFRs generated by each equation by a factor of 5.6 to transform them to total SFRs ($M \geq 0.1M_\odot$) calculated with a Kroupa IMF (Kroupa 2001). The galaxies' SFRs calculated from their thermal and nonthermal fluxes are shown in Table 5 (unresolved galaxies) and Table 6 (resolved galaxies). We report the total massive SFRs of the unresolved galaxies, while we report the massive SFR per square kiloparsec of the resolved galaxies. All of the galaxies for which we calculated both thermal and nonthermal SFRs showed agreement between the two to within an order of magnitude, but not necessarily to within their margins of uncertainty. The disagreement correlates with the thermal fractions of each galaxy: galaxies with high thermal fractions were likely to have higher thermal SFRs than nonthermal SFRs, while galaxies with low thermal fractions showed the opposite relation. Like the differences in thermal fractions between galaxies in our sample, disagreement could be due to the different star formation timescales traced by the thermal and nonthermal fluxes. Since these two emission components are caused by physical processes that operate over differing lengths of time (as discussed in Section 3.3.1), it is possible that the discrepancies between the star formation rates could be used to infer the recent star formation histories of the observed regions.

We compared the radio continuum SFRs to monochromatic SFRs from $24\mu m$ fluxes as described in Calzetti et al. (2010). The galaxies' SFRs (for the unresolved galaxies) and SFR densities (for the resolved galaxies) derived from $24\mu m$ fluxes are listed in Table 5 and Table 6. In Figure 6, we compare the SFRs derived from thermal and nonthermal radio continuum fluxes of the unresolved galaxies for which we fit two-component SEDs to SFRs derived from $24\mu m$ fluxes. We find that most of the galaxies in our sample have higher radio continuum SFRs (both from thermal and nonthermal fluxes) than SFRs from $24\mu m$ data. One possible explanation for this is that extinction is lower at radio wavelengths than it is at $24\mu m$. Another possible explanation is that since radio continuum emission traces very young star formation while $24\mu m$ emission traces less recent star formation, higher SFRs calculated from radio continuum observations than from $24\mu m$ data could be another indication that our sample of galaxies is undergoing recent star formation.

3.7. Radio-far-infrared correlation

There is a well-established tight correlation between far-infrared (FIR) and radio flux in star-forming galaxies (e.g. Helou et al. 1985; Murphy et al. 2006, 2012). When plotted on a log-log scale, the relationship between radio continuum and FIR flux for star-forming galaxies appears linear. This correlation has been well-studied at low frequencies (~ 1.4 GHz) where synchrotron emission is the dominant component of radio emission in a star-forming galaxy. We investigated whether this correlation could also be found on a global scale at 33 GHz, where synchrotron emission is weaker than it is at 1.4 GHz and the relative contribution from thermal emission is more significant.

We limited our study of the radio-FIR correlation to the galaxies in our sample that are unresolved with the GBT beam at 33 GHz (as discussed in Section 2.2). We chose this limit to ensure that we were observing both the total area of radio emission and total area of far-infrared emission in each galaxy. This minimizes issues related to the different beam sizes of the GBT and IRAS (objects are considered point sources to IRAS if they are more compact than $1'$ at 60 μm and $2'$ at 100 μm).

We fit a power law to our 33 GHz flux as a function of total FIR flux. The total FIR flux was determined by a combination of archival IRAS 100 μm and 60 μm fluxes as described in Helou et al. (1988) ($S_{FIR} = 2.58S_{60\mu m} + S_{100\mu m}$). We chose to compute each galaxy's 33 GHz flux by taking the average of its fluxes in the four sub-bands. We used this measure (rather than the flux at 33 GHz inferred from the galaxies' SEDs) in order to eliminate possible uncertainties in the flux due to using assumed spectral indices in our fits. We found that the fluxes were related by $\log S_{33} = (0.88 \pm 0.01)\log S_{FIR} + \log (5.3 \times 10^{-4} \pm 6 \times 10^{-5})$. This correlation is relatively well-fit (the fractional errors of both fit parameters are small) even though our sample contains a wide range of thermal fractions. Murphy et al. (2012) found a similar correlation between 33 GHz and 24μm fluxes for resolved nuclei and individual star-forming regions of galaxies. We find that the radio-FIR correlation at 33 GHz can be extended to global measurements of galaxies' fluxes.

As a control of the tightness of the radio-FIR correlation in our sample, we also fit a relationship between the galaxies' NVSS 1.4 GHz fluxes and their total FIR fluxes. This relationship for the unresolved galaxies in our sample is $\log S_{1.4} = (0.85 \pm 0.01)\log S_{FIR} + \log (0.0047 \pm 0.0006)$. The fractional uncertainties on the fit parameters are similar to those of the fit at 33 GHz. We plot both correlations in Figure 7.

As discussed in Section 3.2, we have determined thermal fractions from SED fits assuming fixed thermal and nonthermal spectral indices. Due to the limited number of radio data points we have for each galaxy, we cannot more accurately constrain the thermal fractions at 33 GHz of the galaxies in our sample at this time. Therefore, we do not have enough information to definitively isolate thermal and nonthermal components to explore whether the radio-FIR correlation is equally tight for each. As an estimate, we have coded approximate thermal fractions in the plot. Even given these limitations, we are confident that a correlation exists between the unresolved galaxies' total radio flux at 33 GHz and total FIR flux. Murphy et al. (2012) found a similar correlation at 33 GHz for resolved nuclei and star-forming regions of galaxies.

To further constrain the radio-FIR correlation at 33 GHz in our sample, we calculated q_ν for each galaxy. q_ν is a logarithmic measure of the ratio of total far-infrared flux (S_{FIR} in Janskys) to radio continuum flux (S_ν) in units of $Wm^{-2}Hz^{-1}$ at a given frequency. It is defined in Helou et al. (1985) as

$$q_\nu = log\left(\frac{S_{FIR} \cdot 1.26 \times 10^{-14} Wm^{-2}}{3.75 \times 10^{12} Wm^{-2}}\right) - log\left(\frac{S_\nu}{Wm^{-2}Hz^{-1}}\right). \tag{6}$$

The average q_{33} for our sample is $q_{33} = 3.3$, with a 1σ scatter of 0.3. Condon (1992) reported that at 1.4 GHz, the average value of $q_{1.4}$ from a large sample of galaxies is $q_{1.4} = 2.3 \pm 0.2$. The average

value of q_ν at 1.4 GHz for this set of galaxies is $q_{1.4} = 2.4 \pm 0.2$, consistent with the Condon (1992) value. Since q_ν is a function of the ratio of FIR flux to radio flux at a given frequency, it makes sense that q_ν is larger using 33 GHz fluxes than it is using 1.4 GHz fluxes (star-forming galaxies are generally much brighter at 1.4 GHz than at 33 GHz). The scatter on q_ν at 33 GHz is larger than that at 1.4 GHZ, which indicates that the radio-FIR correlation is not as tight at 33 GHz as at 1.4 GHz. This may be due to contamination from increased thermal flux at 33 GHz. If the correlation is solely between synchrotron and FIR emission, thermal flux at 33 GHz will increase the scatter in the correlation. However, due to our small sample size, we cannot rule out the possibility that the correlation is just as strong at 33 GHz, where thermal fractions are higher, as it is at 1.4 GHz, where nonthermal emission is typically much stronger. We note that the galaxies with the highest thermal fractions lie above the fitted correlation at 33 GHz, while the same is not true at 1.4 GHz, which supports thermal emission being the cause of increased scatter.

In addition to plotting the radio-FIR correlation, we also plot the ratio of 33 GHz flux to FIR flux, q_{33}^{-1}, against $\alpha_{1.4-33}$ for our unresolved galaxies in Figure 8, similar to Murphy et al. (2012). The plot shows an increasing q_{33}^{-1} for flatter values of $\alpha_{1.4-33}$. Flatter $\alpha_{1.4-33}$ values are presumably indicative of a higher proportion of thermal flux to nonthermal flux, which is reflected in the highest thermal fractions in our sample also having the flattest $\alpha_{1.4-33}$. A correlation between an elevated q_{33}^{-1} and flat values of $\alpha_{1.4-33}$ is not surprising if the radio-FIR correlation is solely dependent on synchrotron emission. If the radio-FIR correlation was independent of the type of radio emission, q_{33}^{-1} should be relatively constant between galaxies and should not be affected by different spectral indices or thermal fractions. Our data support that the radio-FIR correlation is independent of a galaxy's thermal emission since the addition of thermal emission results in elevated ratios of 33 GHz flux to FIR flux.

3.7.1. Implications for star formation timescales

When the timescales of the emission mechanisms for thermal, nonthermal, and FIR fluxes are taken into account, the observed relationship between the ratio of 33 GHz and FIR fluxes and $\alpha_{1.4-33}$ may be a way to age-date an episode of star formation. Since thermal flux is only produced by the shortest-lived ($\tau < 10$ Myr) massive stars, its presence in large quantities relative to synchrotron emission is indicative of very young star formation. Since in addition to massive stars, infrared emission also traces less massive stars ($M > 5M_\odot$) that live longer than the $M > 8M_\odot$ stars that produce thermal and nonthermal radio emission (Devereux & Young 1990), FIR emission is a tracer of star formation on longer timescales. Stars with these masses can live up to ∼100 Myr, while nonthermal radio emission traces stars with lifetimes of up to ∼30 Myr and whose emission is detectable for up to 100 Myr (for an illustrative plot of stellar lifetimes, see Figure 3 of Romano et al. 2005). In addition, infrared emission also contains a component from diffuse dust that is heated by lower-mass stars with lifetimes longer than 100 Myr. These timescales could mean that the galaxies that show both flat spectral indices and enhanced q_{33}^{-1} also host the

youngest areas of ongoing star formation. This correlation could then be a method of determining approximate ages for galaxies' global star formation. As a simple test, we used a Starburst 99 model of a single instantaneous burst using default inputs (solar metallicity, a 2-component Kroupa IMF, and no effects of cosmic ray aging, escape, or absorption taken into account) run for 100 Myr (Leitherer et al. 1999; Vázquez & Leitherer 2005; Leitherer et al. 2010). This model, depicted in Figure 9, shows the flattest spectral indices and highest thermal fractions at the earliest times of the starburst. Similarly, the steepest spectral indices and lowest thermal fractions were seen as the lowest-mass stars that produce supernovae were dying (at $\sim$40 Myr). The starburst's ratio of 33 GHz luminosity to FIR luminosity was also high at early times (between 3 Myr and 40 Myr) while the lowest ratios of 33 GHz luminosity to FIR luminosity were seen even later (after 40 Myr). While modeling a more robust quantitative relationship between this observed correlation and the age of each galaxy's star-forming episode is beyond the scope of this work (the simple model we used does not take into account multiple co-existing generations of star formation), the apparent relationship between enhanced 33 GHz flux, flat spectral indices, and high thermal fractions is a promising metric for future global radio and far-infrared photometric studies of star-forming galaxies. Our simple model is not robust enough to constrain the timescales' uncertainties, but is only meant to be illustrative of a correlation visible in our data.

4. Conclusions

We have observed 27 local, well-studied, star-forming galaxies between 26-40 GHz with the GBT and obtained the first detections at this frequency range for 22 of the galaxies. We determined the contributions of thermal free-free and nonthermal synchrotron emission to the galaxies' total radio emission. We have used these measures to derive the number of massive, short-lived O stars and the number of recent supernovae in the observed regions of each galaxy. In addition, we have calculated SFRs for each galaxy using thermal and nonthermal fluxes and explored the radio-FIR correlation for the unresolved galaxies. We found that

- None of the galaxies have spectral incides indicative of purely thermal emission; eight galaxies show spectra that are too steep to fit thermal components,

- Thermal fractions range from 10% to 90%, with a median of 55%,

- The radio-far infrared correlation holds for the unresolved galaxies at 1.4 GHz and 33 GHz, though the scatter at 33 GHz is larger due to the increased influence of thermal emission at higher frequencies, and

- Galaxies with flat $\alpha_{1.4-33}$ and high thermal fractions have enhanced radio flux at 33 GHz with respect to far-infrared flux, which identifies them as galaxies with recent star formation. This is consistent with a simple model of a single starburst.

We found that the observed regions of our galaxies had a diverse mix of radio continuum characteristics, with some galaxies' SEDs being dominated at 33 GHz by the thermal emission indicative of ongoing massive star formation, while others have little or no detectable thermal emission. Even with this spread in the relative contributions of thermal and nonthermal emission, we saw that there is still a correlation between the global 33 GHz and far-infrared flux in the unresolved galaxies. The scatter in the correlation is larger than that at 1.4 GHz, likely due to the increased influence of thermal emission at 33 GHz. We cannot, however, rule out that the radio-FIR correlation is not solely dependent on synchrotron emission. We also found that higher ratios of 33 GHz emission to FIR emission correlated with flatter spectral indices (and higher thermal fractions) for unresolved galaxies, which is consistent with younger ages in simple starburst models. This correlation may be useful as a rough indicator of the age of the most recent episode of star formation. Future global studies of more homogeneous galaxy populations or resolved studies of individual star-forming regions will enable better modeling of star formation timescales using this metric.

In giving a broad measure of nearby galaxies' radio continuum emission, our observations complement previous studies done with interferometers in which individual star-forming regions in local galaxies were highly resolved. With the GBT, we can simultaneously observe compact and diffuse thermal and nonthermal emission and determine their relative intensities, and in doing so estimate the timescale for the current episode of star formation. Unfortunately, we cannot make stricter timescale estimates than those discussed in Section 3.3 at this time, as we do not have enough radio data points to robustly fit thermal and nonthermal flux components with varying spectral indices. Obtaining more unresolved radio fluxes at lower and higher frequencies would help this effort.

REFERENCES

Aversa, A. G., Johnson, K. E., Brogan, C. L., Goss, W. M., & Pisano, D. J. 2011, AJ, 141, 125

Beck, S. C., Turner, J. L., & Kovo, O. 2000, AJ, 120, 244

Beck, S. C., Turner, J. L., Langland-Shula, L. E., et al. 2002, AJ, 124, 2516

Beck, S. C., Turner, J. L., & Kloosterman, J. 2007, AJ, 134, 1237

Bell, E. F., & de Jong, R. S. 2001, ApJ, 550, 212

Beswick, R. J., Pedlar, A., Clemens, M. S., & Alexander, P. 2003, MNRAS, 346, 424

Calzetti, D., Wu, S.-Y., Hong, S., et al. 2010, ApJ, 714, 1256

Carlstrom, J. E., & Kronberg, P. P. 1991, ApJ, 366, 422

Chyży, K. T., & Beck, R. 2004, A&A, 417, 541

Clemens, M. S., Vega, O., Bressan, A., et al. 2008, A&A, 477, 95

Clemens, M. S., Scaife, A., Vega, O., & Bressan, A. 2010, MNRAS, 405, 887

Condon, J. J. 1992, ARA&A, 30, 575

Condon, J. J., & Yin, Q. F. 1990, ApJ, 357, 97

Devereux, N. A., & Young, J. S. 1990, ApJ, 359, 42

Draine, B. T., & Lazarian, A. 1998, ApJ, 508, 157

Dumas, G., Schinnerer, E., Tabatabaei, F. S., et al. 2011, AJ, 141, 41

Graeve, R., Klein, U., & Wielebinski, R. 1990, A&A, 238, 39

Heesen, V., Beck, R., Krause, M., & Dettmar, R.-J. 2009, A&A, 494, 563

Helou, G., Soifer, B. T., & Rowan-Robinson, M. 1985, ApJ, 298, L7

Helou, G., Khan, I. R., Malek, L., & Boehmer, L. 1988, ApJS, 68, 151

Israel, F. P., & de Bruyn, A. G. 1988, A&A, 198, 109

Johnson, K. E., Indebetouw, R., & Pisano, D. J. 2003, AJ, 126, 101

Johnson, K. E., & Kobulnicky, H. A. 2003, ApJ, 597, 923

Johnson, K. E., Indebetouw, R., Watson, C., & Kobulnicky, H. A. 2004, AJ, 128, 610

Johnson, K. E., Hunt, L. K., & Reines, A. E. 2009, AJ, 137, 3788

Kepley, A. A., Zweibel, E. G., Wilcots, E. M., Johnson, K. E., & Robishaw, T. 2011b, ApJ, 736, 139

Klein, U., Wielebinski, R., & Beck, R. 1984, A&A, 135, 213

Kodilkar, J., Kantharia, N. G., & Ananthakrishnan, S. 2011, MNRAS, 416, 522

Kroupa, P. 2001, MNRAS, 322, 231

Leitherer, C., Schaerer, D., Goldader, J. D., et al. 1999, ApJS, 123, 3

Leitherer, C., Ortiz Otálvaro, P. A., Bresolin, F., et al. 2010, ApJS, 189, 309

Leroy, A. K., Evans, A. S., Momjian, E., et al. 2011, ApJ, 739, L25

Lisenfeld, U., Wilding, T. W., Pooley, G. G., & Alexander, P. 2004, MNRAS, 349, 1335

Maeder, A., & Meynet, G. 1989, A&A, 210, 155

Mason, B. S., Weintraub, L., Sievers, J., et al. 2009, ApJ, 704, 1433

Miller, G. E., & Scalo, J. M. 1979, ApJS, 41, 513

Murphy, E. J., Helou, G., Braun, R., et al. 2006, ApJ, 651, L111

Murphy, E. J., Helou, G., Condon, J. J., et al. 2010, ApJ, 709, L108

Murphy, E. J., Bremseth, J., Mason, B. S., et al. 2012, arXiv:1210.3360

Reines, A. E., Johnson, K. E., & Goss, W. M. 2008, AJ, 135, 2222

Romano, D., Chiappini, C., Matteucci, F., & Tosi, M. 2005, A&A, 430, 491

Rosa-González, D. 2005, MNRAS, 364, 1304

Seaquist, E. R., Bell, M. B., & Bignell, R. C. 1985, ApJ, 294, 546

Tovmassian, H. M. 1972, AJ, 77, 705

Tremonti, C. A., Heckman, T. M., Kauffmann, G., et al. 2004, ApJ, 613, 898

Tsai, C.-W., Turner, J. L., Beck, S. C., et al. 2006, AJ, 132, 2383

Turner, J. L., & Ho, P. T. P. 1994, ApJ, 421, 122

Vacca, W. D., Garmany, C. D., & Shull, J. M. 1996, ApJ, 460, 914

Vázquez, G. A., & Leitherer, C. 2005, ApJ, 621, 695

Table 1. Observation summary

Source	RA [a] (J2000)	Dec (J2000)	D (Mpc)	R_{25} [b] (arcsec)	$R_{23''}$ (kpc)	Hubble Type [c]	# nods [d]	Ref code [e]
NGC 520	01:24:34.8	+03:47:29	30.5 ± 2.1	122.2 ± 3.2	1.7	Sa	2	B03
Maffei II	02:41:55.9	+59:36:14	3.11 ± 0.23	20.8 ± 4.3	0.17	SBbc	2	T94, T06
NGC 1222	03:08:56.8	-02:57:18	32.4 ± 2.3	47.5 ± 3.6	1.8	E/S0	1	B07
SBS 0335-052	03:37:44.0	-05:02:40	53.7 ± 3.8	13.8 [e]	3.0	BCG/starburst [g]	2	J09
IC 342	03:46:48.5	+68:05:46	3.93 ± 0.27	599 ± 3.1	0.22	SABc	1	M12, T06
NGC 1569	04:30:49.3	+64:50:52	1.39 ± 0.11	116.7 ± 3.2	0.08	IB	3	L04
VII Zw 19	04:40:47.3	+67:44:09	67.4 ± 5.5	12.8 ± 3.6	3.8	E	3	B00
NGC 1741	05:01:38.3	-04:15:24	54.6 ± 3.8	36.1 ± 3.6	3.0	Sm	1	B00
II Zw 40	05:55:42.6	+03:23:32	11.1 ± 0.80	16.8 [f]	0.62	Sbc	3	B02
Mrk 8	07:29:26.3	+72:07:44	52.5 ± 3.7	26.1 ± 4.1	2.9	Sbc	1	B00
Mrk 86	08:13:14.6	+45:59:29	7.94 ± 1.5	61.3 ± 3.4	0.44	SBm	1	A11
NGC 2903	09:32:09.7	+21:30:02	7.39 ± 0.52	360.8 ± 3.1	0.41	SABb	1	T06
NGC 2997	09:45:38.7	-31:11:25	13.8 ± 0.90	307.0 ± 3.1	0.77	SABc	1	K11
Mrk 1236	09:49:54.1	+00:36:58	27.6 ± 5.1	36.1 ± 3.3	1.5	WR/HII [g]	1	B00
NGC 3077	10:03:20.2	+68:44:01	2.55 ± 0.19	157.4 ± 3.2	0.14	S?	1	M12, R05
NGC 3125	10:06:33.6	-29:56:08	13.8 ± 1.0	36.1 ± 3.3	0.77	E	1	A11
Arp 233	10:32:31.1	+54:24:04	25.5 ± 1.8	34.4 ± 3.4	1.4	I	1	T72, B00, A11
Arp 217	10:38:45.9	+53:30:11	19.2 ± 1.3	57.2 ± 3.3	1.1	SABb	1	A11
Haro 3	10:45:22.4	+55:57:37	18.5 ± 1.3	40.5 ± 3.4	1.0	Sb	1	T72, J04, A11
Pox 4	11:51:11.7	-20:35:57	52.5 ± 3.9	19.4 ± 3.4	2.9	Sm	1	B00
NGC 4038	12:01:52.5	-18:52:02	21.5 ± 1.6	161.1 ± 3.2	1.2	SBm	1	C04
NGC 4214	12:15:39.2	+36:19:41	2.94 ± 0.27	202.8 ± 3.2	0.16	IB	1	B00
NGC 4449	12:28:10.1	+44:05:33	3.54 ± 0.25	140.3 ± 3.2	0.20	IB	1	R08

Table 1—Continued

Source	RA [a] (J2000)	Dec (J2000)	D (Mpc)	R_{25} [b] (arcsec)	$R_{23''}$ (kpc)	Hubble Type [c]	# nods [d]	Ref code [e]
NGC 4490	12:30:36.7	+41:38:26	9.22 ± 0.65	202.8 ± 3.3	0.51	SBcd	1	A11
Tol 35	13:27:07.2	-27:57:26	25.2 ± 1.8	43.4 ± 3.4	1.4	Sab	1	B00
M 51	13:29:52.4	+47:11:40	7.90 ± 0.85	414.1 ± 3.1	0.44	Sbc	1	M12, T94, D11
M 101	14:03:12.5	+54:20:53	6.46 ± 0.18	719.7 ± 3.1	0.36	SABc	1	M12, T94

[a]RA and Dec are center positions of the beam for each observation.

[b]R_{25} values are derived from average d_{25} from Hyperleda (http://leda.univ-lyon1.fr/).

[c]Hubble types from Hyperleda except where specified.

[d]Each nod is 70 seconds long.

[e]These galaxies have previously published radio continuum observations. M12 denotes galaxies detected with the CCB by Murphy et al. (2012) at 33 GHz. T72 denotes galaxies that were observed, but not detected, by Tovmassian (1972) at 9.5 mm (31.6 GHz). T94 (Turner & Ho 1994), B00 (Beck et al. 2000), B02 (Beck et al. 2002), B03 (Beswick et al. 2003), C04 (Chyży & Beck 2004), J04 (Johnson et al. 2004), L04 (Lisenfeld et al. 2004), R05 (Rosa-González 2005), T06 (Tsai et al. 2006), B07 (Beck et al. 2007), R08 (Reines et al. 2008), J09 (Johnson et al. 2009), D11 (Dumas et al. 2011), K11 (Kodilkar et al. 2011), and A11 (Aversa et al. 2011) denote galaxies that were observed at lower frequencies. The galaxies are described in more detail in these papers.

[f]No radius data available from Hyperleda so major axis diameter from NED is reported.

[g]No Hubble type data available from Hyperleda so classification listed on NED is reported.

Table 2.   Observed Flux

Source	27.75 GHz (mJy)	31.25 GHz (mJy)	34.75 GHz (mJy)	38.25 GHz (mJy)
Four-sub-band detections: flux in each sub-band				
NGC 520	21.77 ± 0.39	19.50 ± 0.19	17.44 ± 0.27	15.43 ± 0.43
Maffei II	23.17 ± 0.28	19.42 ± 0.16	16.36 ± 0.20	13.98 ± 0.29
NGC 1222	9.83 ± 0.53	8.57 ± 0.25	7.91 ± 0.36	7.26 ± 0.54
SBS 0335-052	0.66 ± 0.20	0.62 ± 0.12	0.69 ± 0.18	0.52 ± 0.24
IC 342	35.59 ± 3.46	31.03 ± 0.87	27.82 ± 1.08	25.25 ± 2.21
NGC 1569	28.60 ± 0.19	24.67 ± 0.12	21.31 ± 0.15	18.75 ± 0.21
VII Zw 19	3.16 ± 0.27	2.60 ± 0.14	2.26 ± 0.19	2.11 ± 0.27
NGC 1741	2.12 ± 0.31	2.07 ± 0.18	1.67 ± 0.22	0.84 ± 0.32
II Zw 40	15.09 ± 2.00	14.12 ± 0.50	12.99 ± 0.62	12.20 ± 1.28
Mrk 8	3.23 ± 0.38	2.84 ± 0.39	2.21 ± 0.33	2.53 ± 0.42
NGC 2903	14.50 ± 1.47	12.80 ± 0.52	11.15 ± 0.82	9.60 ± 1.16
NGC 2997	5.14 ± 1.12	4.77 ± 0.45	4.38 ± 0.63	3.90 ± 0.85
NGC 3077	6.94 ± 0.39	5.93 ± 0.38	5.45 ± 0.32	4.71 ± 0.43
NGC 3125	8.15 ± 1.03	7.43 ± 0.44	6.52 ± 0.58	5.92 ± 0.79
Arp 233	4.22 ± 0.43	4.05 ± 0.40	3.49 ± 0.31	2.93 ± 0.43
Arp 217	25.98 ± 0.43	21.65 ± 0.40	19.04 ± 0.31	16.26 ± 0.43
Haro 3	6.10 ± 0.43	5.49 ± 0.40	4.78 ± 0.31	4.35 ± 0.43
NGC 4038	7.77 ± 0.96	5.44 ± 0.42	4.64 ± 0.55	4.27 ± 0.74
NGC 4214	7.18 ± 0.93	6.22 ± 0.38	5.26 ± 0.48	4.68 ± 0.69
NGC 4449	4.37 ± 0.90	3.45 ± 0.38	2.73 ± 0.44	2.30 ± 0.65
NGC 4490	3.40 ± 0.90	2.64 ± 0.38	1.64 ± 0.46	1.33 ± 0.66
M 51	7.67 ± 0.94	5.84 ± 0.38	4.89 ± 0.47	3.65 ± 0.65
Marginal detections: average of four sub-bands' fluxes				
Mrk 86	0.42 ± 0.19			
Mrk 1236	0.99 ± 0.40			
Pox 4	1.62 ± 0.29			
Tol 35	< 0.87			
M 101[b]	0.69 ± 0.27			

[a]α_{26-40} is calculated using the 27.75 GHz and 38.25 GHz fluxes.

[b]The lower-frequency radio continuum emission of M 101 is more extended than the separation between the on-source and off-source beams (Graeve et al. 1990), so its reported flux may suffer from oversubtraction due to emission in the off-source beam.

Table 3.   Beam correction factors for galaxies detected in all four sub-bands

Source Beamsize	27.75 GHz 26.7 $''$	31.25 GHz 23.7 $''$	34.75 GHz 21.3 $''$	38.25 GHz 19.4 $''$
NGC 520	0.99	0.99	1	1.01
Maffei II	0.89	0.95	1	1.05
NGC 1222[a]	$\cdots$	$\cdots$	$\cdots$	$\cdots$
SBS 0335-052	0.98	0.99	1	1.01
IC 342	0.93	0.97	1	1.03
NGC 1569	0.81	0.91	1	1.09
VII Zw 19	0.97	0.99	1	1.02
NGC 1741	0.98	0.99	1	1.01
II Zw 40	0.95	0.97	1	1.03
Mrk 8	0.92	0.96	1	1.04
NGC 2903	0.96	0.98	1	1.03
NGC 2997	0.89	0.94	1	1.07
NGC 3077	0.97	0.98	1	1.02
NGC 3125	0.92	0.96	1	1.04
Arp 233	0.98	0.99	1	1.01
Arp 217	0.87	0.93	1	1.07
Haro 3	0.95	0.98	1	1.03
NGC 4038	0.83	0.94	1	1.03
NGC 4214	0.87	0.94	1	1.07
NGC 4449	0.78	0.89	1	1.11
NGC 4490	0.75	0.87	1	1.13
M 51	0.83	0.91	1	1.08
average	0.91	0.95	1	1.05
standard dev	0.07	0.04	0	0.04

[a]NGC 1222 did not have archival radio data available for re-imaging, so average beam correction values were used.

Table 4.   Corrected Flux

Source	27.75 GHz (mJy)	31.25 GHz (mJy)	34.75 GHz (mJy)	38.25 GHz (mJy)	α_{26-40}[a]	Notes[b]
Four-port detections: flux in each port						
NGC 520	21.54 ± 0.39	19.30 ± 0.19	17.44 ± 0.27	15.58 ± 0.43	-1.01 ± 0.10	
Maffei II	20.62 ± 0.28	18.45 ± 0.16	16.36 ± 0.20	14.68 ± 0.29	-1.06 ± 0.07	1
NGC 1222	8.94 ± 0.53	8.14 ± 0.25	7.91 ± 0.36	7.62 ± 0.54	-0.50 ± 0.29	2
SBS 0335-052	0.65 ± 0.20	0.61 ± 0.12	0.69 ± 0.18	0.53 ± 0.24	-0.65 ± 1.7	
IC 342	33.10 ± 3.5	30.10 ± 0.87	27.82 ± 1.1	26.01 ± 2.2	-0.75 ± 0.42	
NGC 1569	23.17 ± 0.19	22.45 ± 0.12	21.31 ± 0.15	20.44 ± 0.21	-0.39 ± 0.04	1
VII Zw 19	3.07 ± 0.27	2.54 ± 0.14	2.26 ± 0.19	2.15 ± 0.27	-1.10 ± 0.48	
NGC 1741	2.08 ± 0.31	2.05 ± 0.18	1.67 ± 0.22	0.85 ± 0.32	-2.78[2]± 1.3	
II Zw 40	14.33 ± 2.0	13.70 ± 0.50	12.99 ± 0.62	12.59 ± 1.3	-0.41 ± 0.54	
Mrk 8	2.97 ± 0.38	2.72 ± 0.39	2.21± 0.33	2.63± 0.42	-0.38 ± 0.64	
NGC 2903	13.91 ± 1.5	12.54 ± 0.52	11.15 ± 0.82	9.89 ± 1.2	-1.06 ± 0.51	
NGC 2997	4.58 ± 1.1	4.48 ± 0.45	4.38 ± 0.63	4.17 ± 0.85	-0.29 ± 0.98	1
NGC 3077	6.73 ± 0.39	5.81 ± 0.38	5.45 ± 0.32	4.80 ± 0.43	-1.05 ± 0.33	
NGC 3125	7.49 ± 1.0	7.13 ± 0.44	6.52 ± 0.58	6.15 ± 0.79	-0.62 ± 0.58	
Arp 233	4.14 ± 0.43	4.01 ± 0.40	3.49 ± 0.31	2.96 ± 0.43	-1.05 ± 0.56	
Arp 217	22.60 ± 0.43	20.14 ± 0.40	19.04 ± 0.31	17.40 ± 0.43	-0.81 ± 0.10	
Haro 3	5.79 ± 0.43	5.38 ± 0.40	4.78 ± 0.31	4.48 ± 0.43	-0.80 ± 0.38	
NGC 4038	6.45 ± 0.96	5.11 ± 0.42	4.64 ± 0.55	4.39 ± 0.74	-1.20 ± 0.70	1
NGC 4214	6.25 ± 0.93	5.84 ± 0.38	5.26 ± 0.48	5.01 ± 0.69	-0.69 ± 0.63	1
NGC 4449	3.41 ± 0.90	3.07 ± 0.38	2.73 ± 0.44	2.56 ± 0.65	-0.90 ± 1.1	1
NGC 4490	2.55 ± 0.90	2.30 ± 0.38	1.64 ± 0.46	1.50 ± 0.66	-1.65 ± 1.8	1
M 51	6.36 ± 0.94	5.32 ± 0.38	4.89 ± 0.47	3.94 ± 0.65	-1.49 ± 0.69	1,3

[a]α_{26-40} is calculated using the 27.75 GHz and 38.25 GHz fluxes.

[b]Notes: 1: Lower-frequency radio continuum emission is more extended than the largest beam. 2: No lower-frequency radio continuum emission available; used characteristic beam-size correction values. 3: The lower-frequency radio continuum emission of M 51 is more extended than the separation between the on-source and off-source beams (Klein et al. 1984), so its reported flux may suffer from oversubtraction due to emission in the off-source beam.

[c]Though α_{26-40} for NGC 1741 is extremely steep (determining α_{26-40} via calculation and via a fit both result in $\alpha_{26-40} < -2$), its SED can be fit with a spectral index of $\alpha = -0.8$ when a 1.4 GHz data point is incorporated into the fit.

Table 5.   Star formation properties of unresolved galaxies

Source	Thermal fraction [a]	Log max # O7.5V stars	Log SNe rate (yr^{-1})	Thermal SFR [b] $(M_\odot yr^{-1})$	Nonthermal SFR [c] $(M_\odot yr^{-1})$	Infrared SFR [d] $(M_\odot yr^{-1})$
NGC 520	0.24 ± 0.01	4.65	-0.71	7.16 ± 0.43	26.7 ± 3.7	5.99 ± 0.94
NGC 1222	0.43 ± 0.02	4.59	-1.14	6.26 ± 0.48	9.8 ± 1.4	5.03 ± 0.79
SBS0335-052	0.79 ± 0.06	4.18	-2.25	2.43 ± 0.50	0.77 ± 0.25	$\cdots$
IC 342	0.53 ± 0.02	3.41	-2.50	0.41 ± 0.03	0.43 ± 0.06	0.60 ± 0.09
VII Zw 19	0.38 ± 0.003	4.66	-0.97	7.28 ± 0.07	14.4 ± 2.3	16.6 ± 3.0
NGC 1741	< 1.00	< 4.87	-1.03	< 12.0	12.7 ± 1.8	3.80 ± 0.62
II Zw 40	0.91 ± 0.01	4.20	-2.63	2.57 ± 0.09	0.32 ± 0.05	0.46 ± 0.08
Mrk 8	0.50 ± 0.05	4.58	-1.26	6.1 ± 1.1	7.4 ± 1.2	2.19 ± 0.38
NGC 2903	< 0.94	< 3.90	-1.92	< 1.28	1.62 ± 0.23	0.31 ± 0.05
NGC 3077	0.66 ± 0.02	2.42	-3.72	0.042 ± 0.003	0.026 ± 0.004	0.0022 ± 0.004
NGC 3125	0.77 ± 0.02	4.03	-2.35	1.73 ± 0.11	0.61 ± 0.10	0.30 ± 0.06
Arp 233	0.71 ± 0.02	4.25	-1.99	2.89 ± 0.22	1.40 ± 0.21	1.29 ± 0.21
Arp 217	< 0.99	< 4.92	-0.92	< 13.4	16.2 ± 2.1	3.71 ± 0.61
Haro 3	0.85 ± 0.02	4.19	-2.40	2.51 ± 0.13	0.54 ± 0.10	0.65 ± 0.11
Marginal Detections						
Mrk 86	$\cdots$	< 2.82	< -3.02	< 0.11	< 0.13	0.037 ± 0.015
Mrk 1236	$\cdots$	< 4.25	< -1.60	< 2.88	< 3.43	0.36 ± 0.15
Pox 4	$\cdots$	< 4.87	< -0.98	< 11.8	< 14.1	0.87 ± 0.27
Tol 35	$\cdots$	< 3.99	< -1.86	< 1.57	< 1.87	$\cdots$

[a]The thermal fractions of each galaxy at 33 GHz are based on two-component fits, except for the galaxies with negative fitted thermal components. In such cases, the thermal fractions are presented as 3σ upper limits.

[b]Thermal SFRs are calculated using thermal flux following Equation 4 scaled to a Kroupa IMF.

[c]Nonthermal SFRs are calculated using nonthermal flux following Equation 5 scaled to a Kroupa IMF.

[d]Infrared SFRs are calculated from IRAS $24\mu m$ fluxes using Equations 1 and 17 of Calzetti et al. (2010).

Table 6.   Star formation properties of resolved galaxies

Source	Thermal fraction [a]	Log max # O7.5V stars (kpc^{-2})	Log SNe rate $(yr^{-1}kpc^{-2})$	Thermal SFR density [b] $(M_\odot yr^{-1}kpc^{-2})$	Nonthermal SFR density [c] $(M_\odot yr^{-1}kpc^{-2})$	Infrared SFR density [d] $(M_\odot yr^{-1}kpc^{-2})$
MaffeiII	< 0.97	< 4.27	-1.57	< 2.99	3.69 ± 0.77	0.039 ± 0.009
NGC 1569	0.11 ± 0.03	3.41	-1.52	0.41 ± 0.15	4.06 ± 0.92	0.31 ± 0.07
NGC 2997	0.32 ± 0.01	3.19	-2.34	0.25 ± 0.04	0.63 ± 0.12	⋯
NGC 4038	< 0.87	< 3.84	-1.95	< 1.11	1.53 ± 0.33	⋯
NGC 4214	0.58 ± 0.03	3.55	-2.44	0.56 ± 0.12	0.49 ± 0.13	0.076 ± 0.022
NGC 4449	< 1.00	< 3.65	-2.25	< 0.72	0.76 ± 0.15	⋯
NGC 4490	< 0.92	< 3.52	-2.29	< 0.53	0.69 ± 0.15	0.16 ± 0.04
M 51	< 0.94	< 3.84	-1.98	< 1.11	1.41 ± 0.43	0.13 ± 0.04
Marginal Detection						
M 101	⋯	< 2.83	< -3.02	< 0.26	< 0.32	0.015 ± 0.002

[a]The thermal fractions of each galaxy at 33 GHz are based on two-component fits, except for the galaxies with negative fitted thermal components. In such cases, the thermal fractions are presented as 3σ upper limits.

[b]Thermal SFR densities are calculated using thermal flux following Equation 4 and scaled to a Kroupa IMF over the area of the 23″ GBT beam.

[c]Nonthermal SFR densities are calculated using nonthermal flux following Equation 5 and scaled to a Kroupa IMF over the area of the 23″ GBT beam.

[d]Infrared SFR densities are calculated from IRAS $24\mu m$ fluxes using Equations 1 and 17 of Calzetti et al. (2010) over the area of the 47″ IRAS beam at $25\mu m$.

Table 7. Radio and far-infrared properties of unresolved galaxies

Source	33 GHz flux[a] (mJy)	1.4 GHz flux[b] (mJy)	Far-IR flux[c] (Jy)	$\alpha_{1.4-33}$	q_{33}[d]
NGC 520	18.5 ± 0.2	176.3 ± 5.3	129.72 ± 0.04	-0.71 ± 0.01	3.37 ± 0.004
NGC 1222	8.15 ± 0.22	61.7 ± 1.9	47.89 ± 0.01	-0.64 ± 0.01	3.30 ± 0.01
SBS 0335-052	0.62 ± 0.04	2.3 ± 0.4	$\cdots$	-0.41 ± 0.06	$\cdots$
IC 342	29.3 ± 1.1	190.7 ± 7.3	348.22 ± 0.03	-0.59 ± 0.02	3.60 ± 0.02
VII Zw 19	2.51 ± 0.11	20.5 ± 0.7	18.97 ± 0.03	-0.66 ± 0.02	3.40 ± 0.02
NGC 1741	1.66 ± 0.13	30.4 ± 1.6	16.13 ± 0.02	-0.92 ± 0.03	3.51 ± 0.03
II Zw 40	13.4 ± 0.6	32.5 ± 1.1	22.87 ± 0.03	-0.28 ± 0.02	2.76 ± 0.02
Mrk 8	2.63 ± 0.19	18.1 ± 1.0	348.22 ± 0.03	-0.61 ± 0.03	3.11 ± 0.03
Mrk 86	0.42 ± 0.19	10.5 ± 1.7	14.75 ± 0.03	-1.02 ± 0.15	4.07 ± 0.20
NGC 2903	11.9 ± 0.5	444.5 ± 13.9	176.93 ± 0.03	-1.14 ± 0.02	3.70 ± 0.02
Mrk 1236	0.99 ± 0.40	16.5 ± 1.8	11.03 ± 0.03	-0.89 ± 0.13	3.57 ± 0.18
NGC 3077	5.70 ± 0.19	29.0 ± 1.5	61.65 ± 0.02	-0.51 ± 0.02	3.56 ± 0.01
NGC 3125	6.82 ± 0.37	26.6 ± 1.6	19.31 ± 0.03	-0.43 ± 0.03	2.98 ± 0.02
Arp 233	3.65 ± 0.20	16.6 ± 0.6	17.84 ± 0.03	-0.48 ± 0.02	3.22 ± 0.02
Arp 217	19.8 ± 0.2	362.8 ± 12.4	127.65 ± 0.03	-0.92 ± 0.01	3.34 ± 0.004
Haro 3	5.11 ± 0.20	15.5 ± 0.9	19.51 ± 0.02	-0.35 ± 0.02	3.11 ± 0.02
Pox 4	1.62 ± 0.29	4.2 ± 0.5	$\cdots$	-0.30 ± 0.07	$\cdots$

[a]The 33 GHz flux is the average of the corrected fluxes in the four sub-bands.

[b]The 1.4 GHz flux is taken from the NRAO VLA Sky Survey.

[c]The far-IR flux is derived from IRAS $60\mu m$ and $100\mu m$ fluxes using $S_{FIR} = 2.58 S_{60\mu m} + S_{100\mu m}$ (Helou et al. 1988).

[d]q_{33} is a logarithmic measure of the ratio of far-IR flux (in Jy) to 33 GHz flux (in $Wm^{-2}Hz^{-1}$).
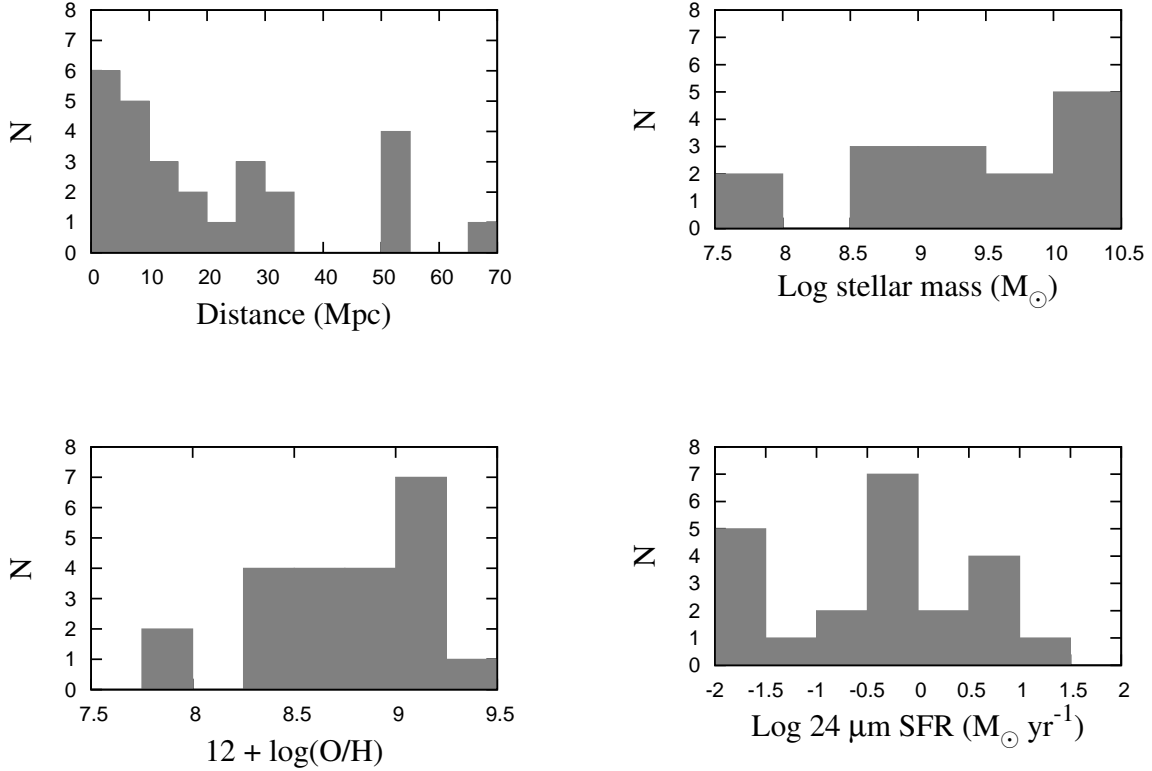
Fig. 1.—: *Top Left:* Distribution of distances in our sample. *Top Right:* Distribution of K band optical galactic stellar masses in our sample estimated using the (B-V) color and the expression in Bell & de Jong (2001). *Bottom Left:* Metallicity distribution for our sample estimated from the B band absolute magnitude using the expression in Tremonti et al. (2004). *Bottom Right:* Star formation rate for galaxies in our sample calculated using the 25μm IRAS fluxes for our sample and the expression in Calzetti et al. (2010). Not all galaxies are represented in every histogram.
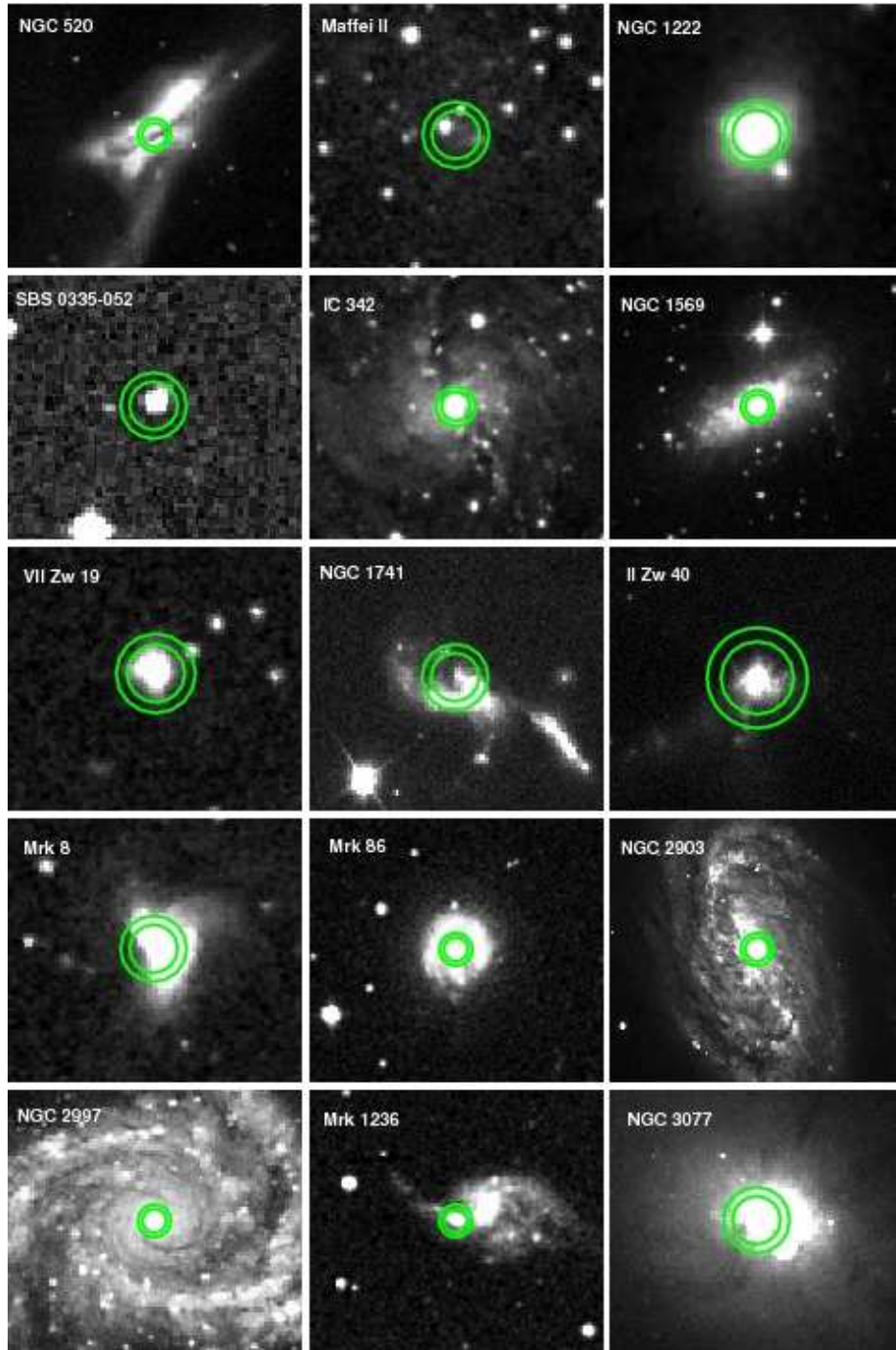
Fig. 2.—: Largest ($\sim 27''$) and smallest ($\sim 19''$) beam sizes overlaid on SDSS g or DSS B images of each galaxy observed. The galaxies are presented in the order listed in Table 1 viewed left to right and top to bottom.
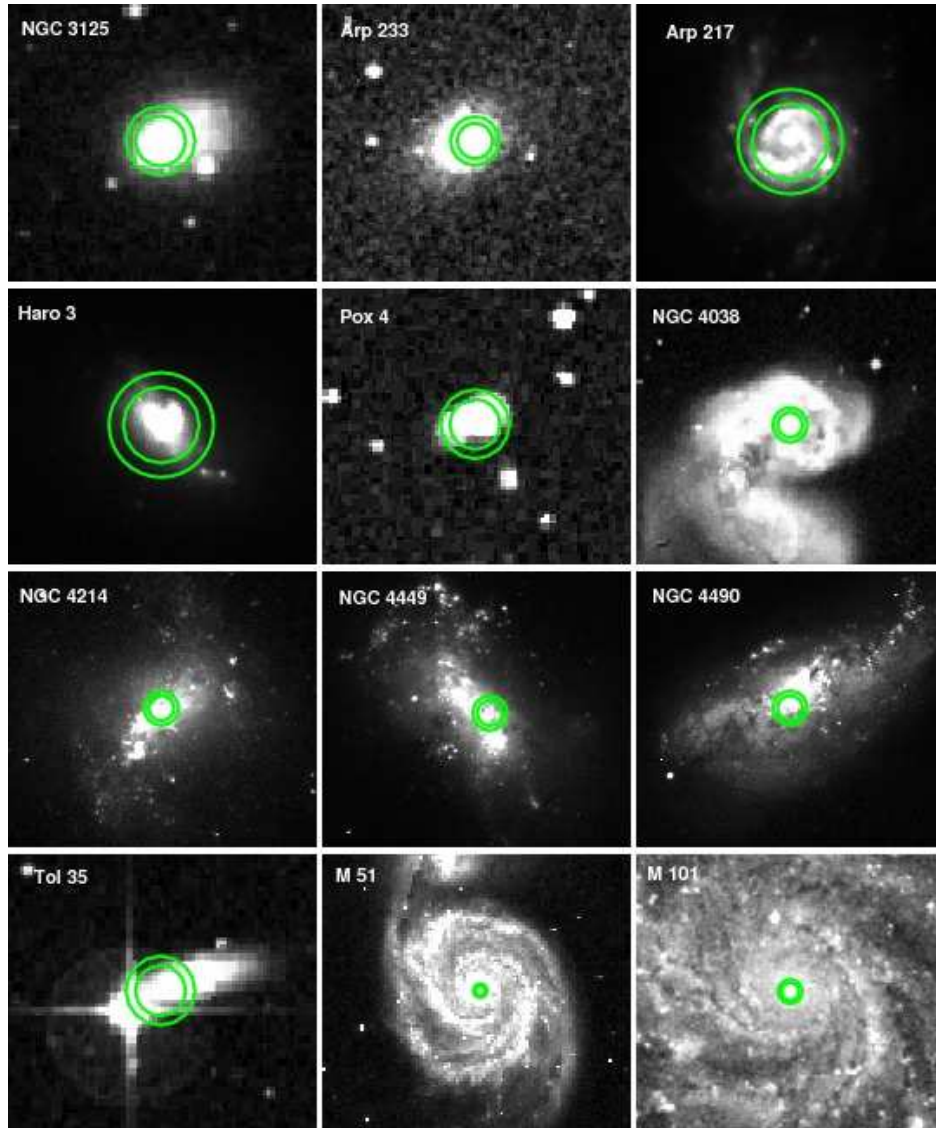
Fig. 2.—: Continued.
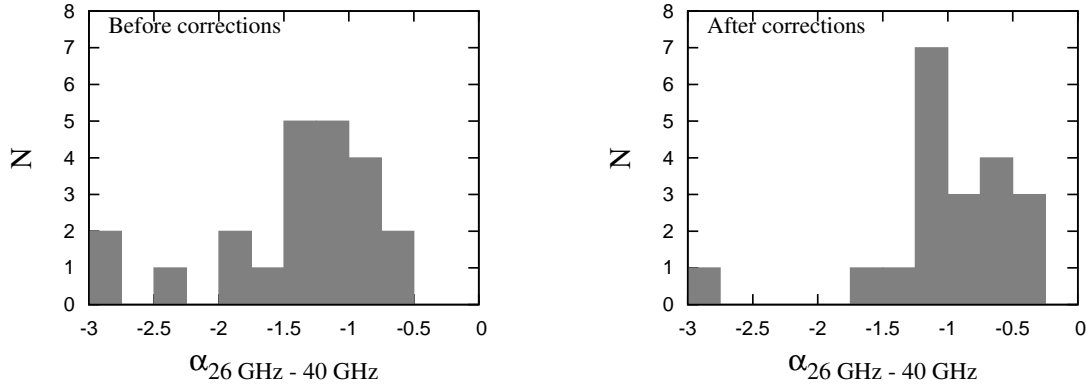
Fig. 3.—: Distribution of α_{26-40} before correcting for beam size (left) and after the corrections have been applied (right). The beam size corrections flatten α_{26-40} relative to uncorrected data.
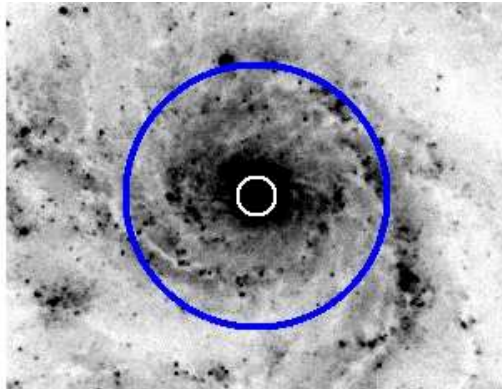
Fig. 4.—: Average CCB beamsize ($\sim 23''$, white) and circle with radius ($\sim 78''$) equal to the separation between the "on" and "off" beams (blue) overlaid on an optical (SDSS g) image of M 101. M 101 and M 51 are both larger than the beam separation, which likely results in an oversubtraction when the flux in the "off" beam is subtracted from the flux in the "on" beam.
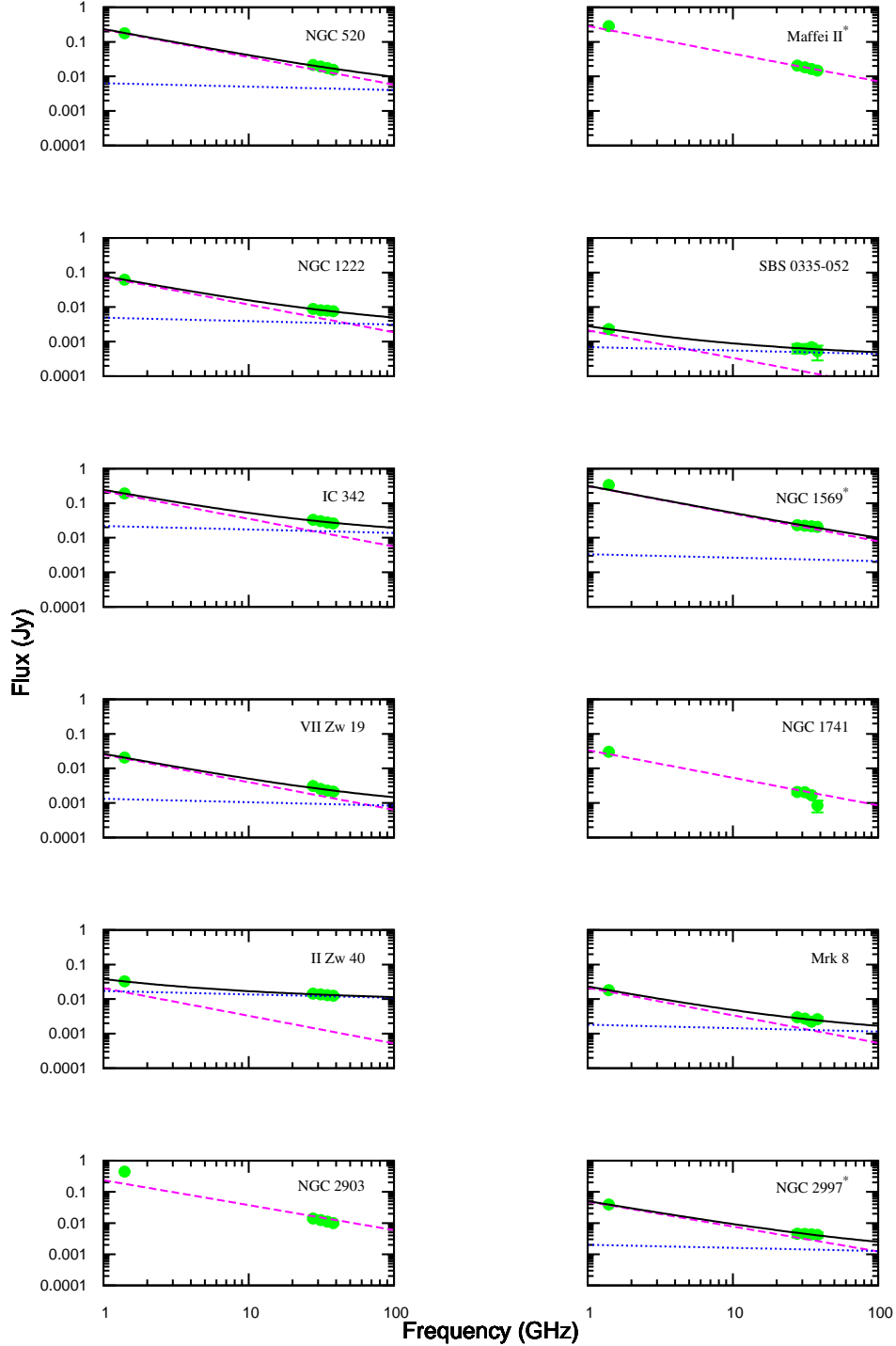
Fig. 5.—: NVSS 1.4 GHz and CCB 26-40 GHz points for each galaxy that was detected with all four CCB subbands. In most cases, the error bars are smaller than the point size. The best-fit spectral energy distribution for each galaxy is also plotted. Each SED was fit with a combination of nonthermal and thermal components (black line). The purple dashed line is the nonthermal ($\alpha_N = -0.8$) component, the blue dotted line is the thermal ($\alpha_T = -0.1$) component. When a galaxy's SED could not be fit with the inclusion of a positive thermal component, we only fit the nonthermal component (the thermal flux at 33 GHz is calculated as an upper limit in such cases). Galaxies that are resolved at 33 GHz are marked with an *.
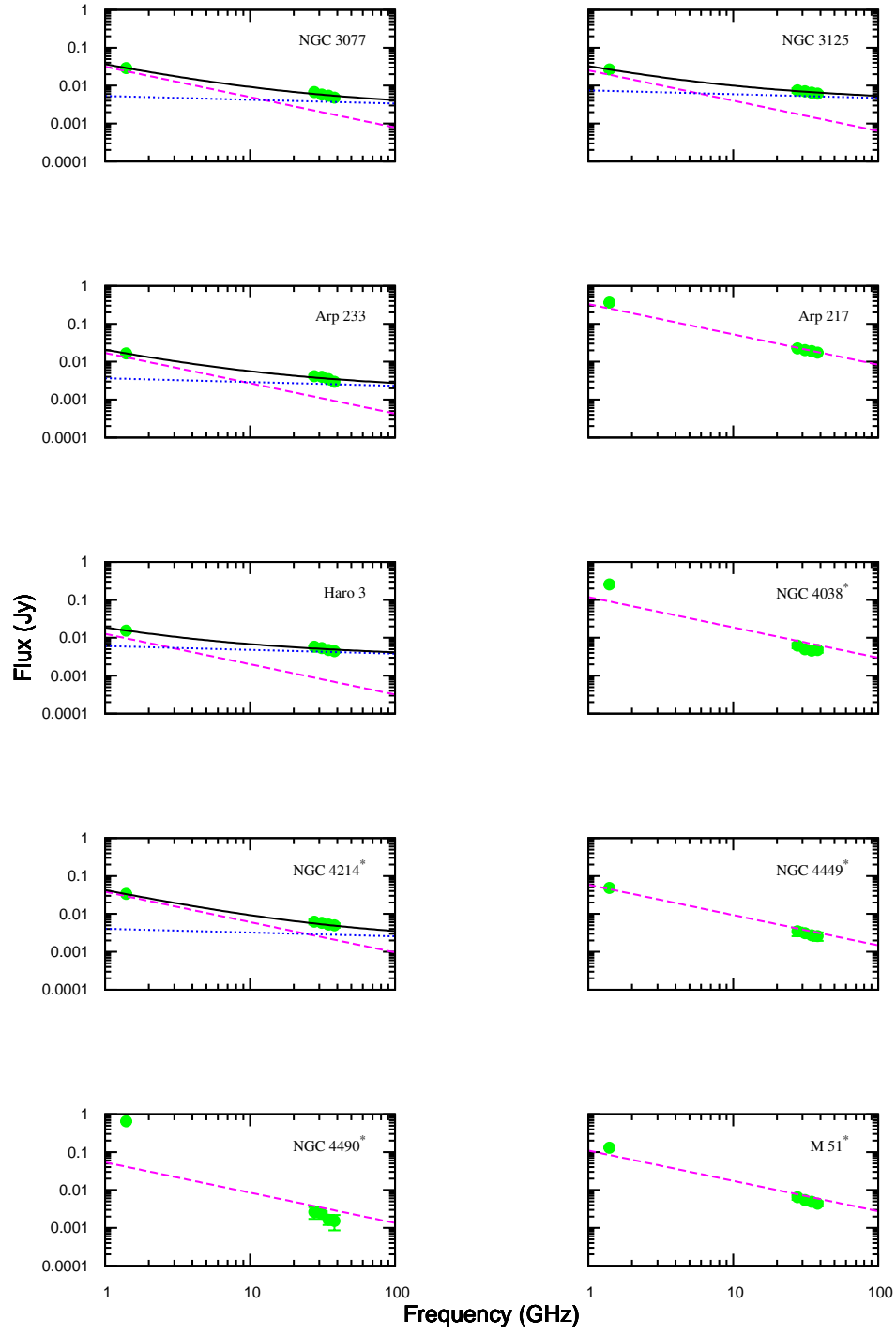
Fig. 5.—: Continued.
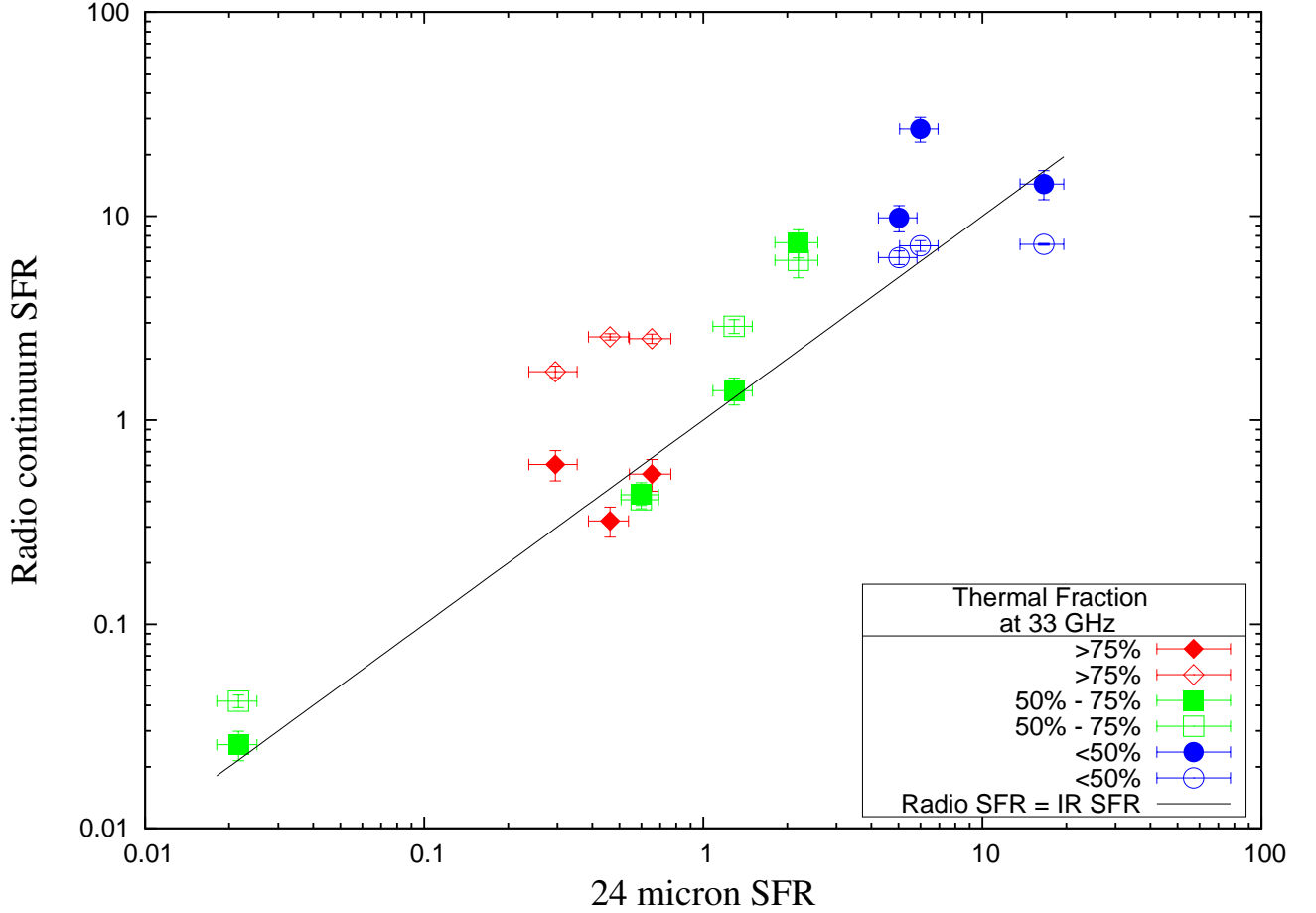
Fig. 6.—: Star formation rates calculated from nonthermal (filled symbols) and thermal (open symbols) radio continuum fluxes plotted against SFRs calculated from IRAS $25\mu m$ fluxes according to Equations 1 and 17 from Calzetti et al. (2010). The solid black line represents equal SFRs at radio and infrared wavelengths. Most galaxies have higher SFRs when calculated using radio continuum fluxes, which trace more recent star formation than infrared fluxes.
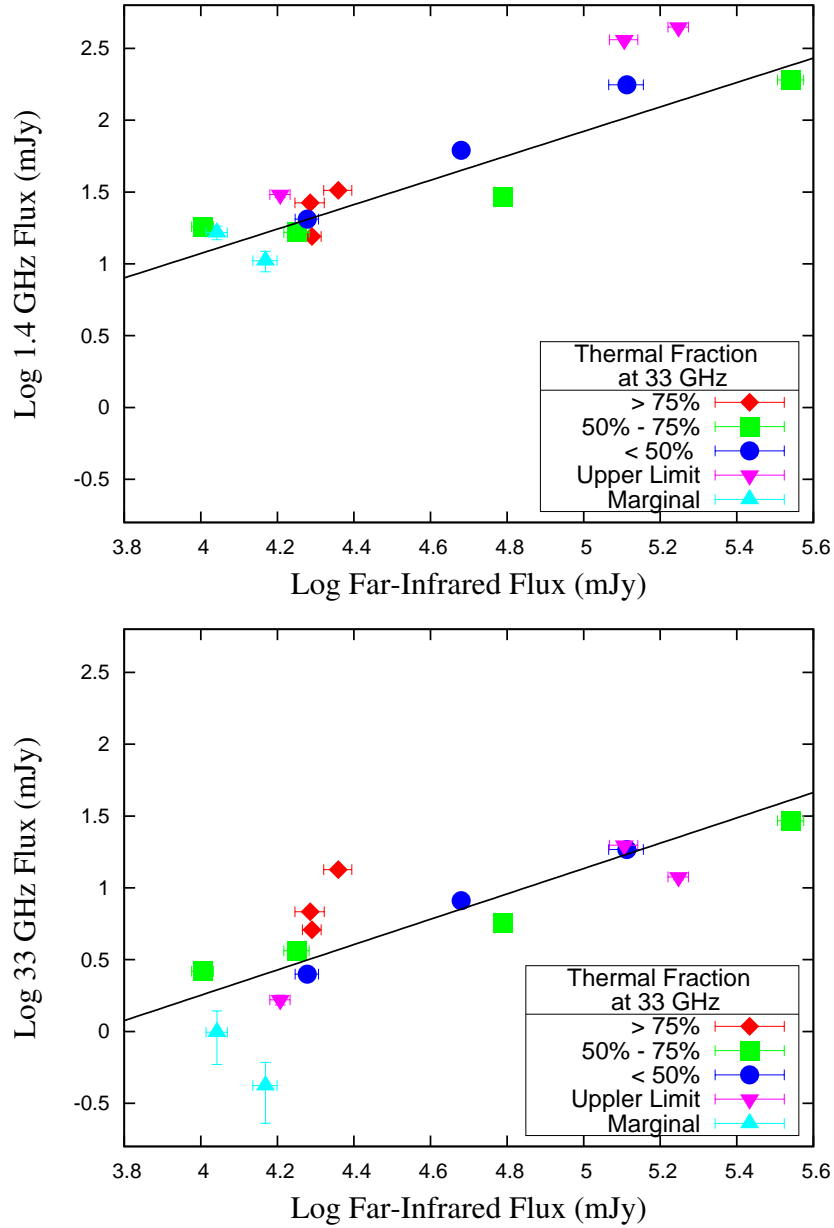
Fig. 7.—: Radio-far-infrared correlation for 1.4 GHz (top) and 33 GHz (bottom) fluxes vs. total far-infrared flux. The FIR flux is derived from a combination of IRAS 60 μm and 100 μm data. All of the galaxies unresolved with the GBT's 23″ beam are plotted except for SBS 0335-052, which was not detected by IRAS, and Pox 4, which was not detected at 100 μm. The lines that best fit each data set are also plotted. The galaxies are coded by thermal fraction at 33 GHz. While the correlation is tighter at 1.4 GHz than it is at 33 GHz, it is still easily seen at 33 GHz. Since the galaxies with the highest thermal fractions all lie above the best-fit line at 33 GHz (but don't at 1.4 GHz), it is possible that some of the scatter in the correlation at 33 GHz is due to the increased proportion of thermal emission at higher frequencies.
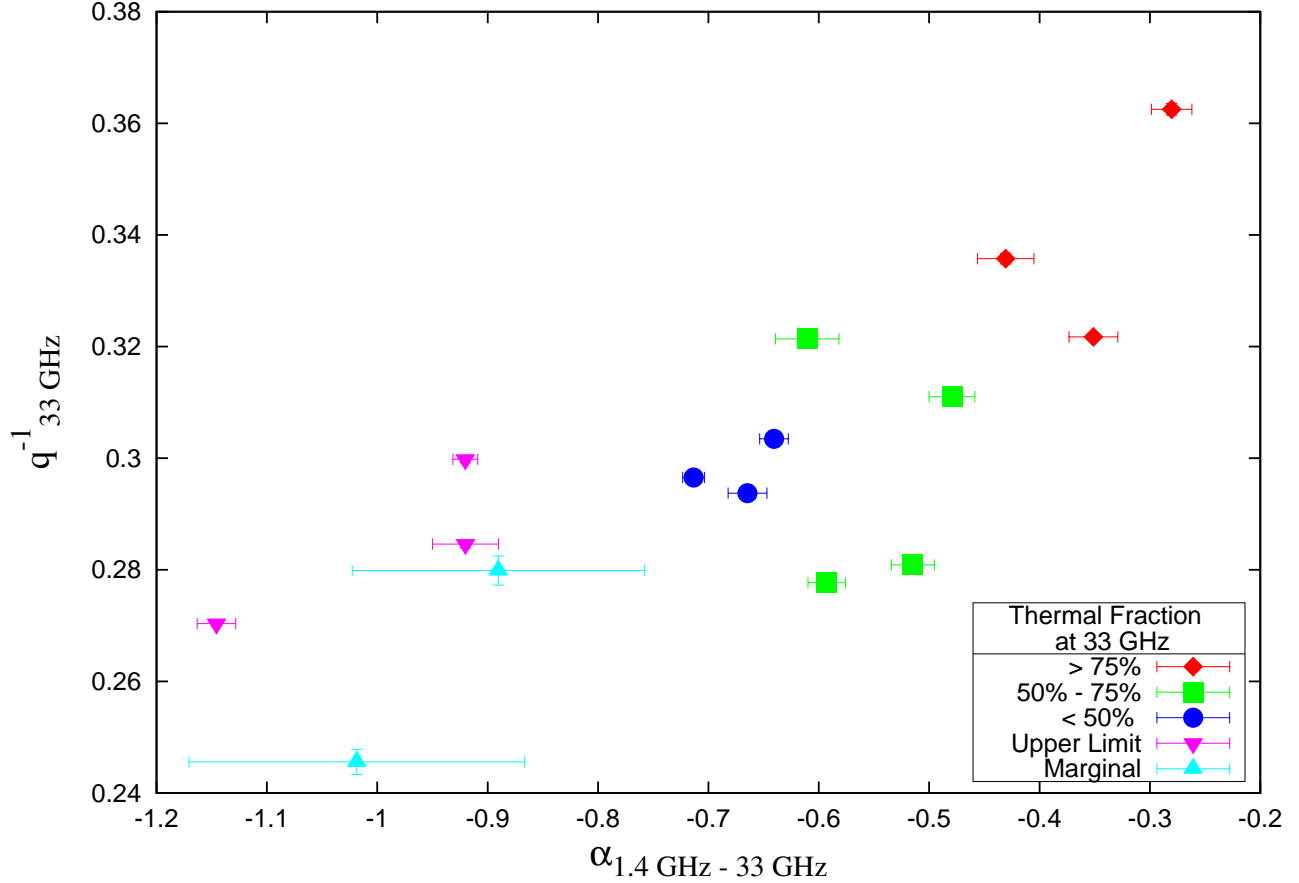
Fig. 8.—: q_{33}^{-1} vs $\alpha_{1.4-33}$ using 33 GHz fluxes for unresolved galaxies. q_{ν}^{-1} is a measure of the ratio between radio flux and total far-infrared flux at a given radio frequency. As in Figure 7, SBS 0335-052 and Pox 4 are not plotted. The red diamonds represent the highest thermal fraction (greater than 75%). The green squares represent galaxies with thermal fractions between 50% and 75%. The blue circles represent galaxies with thermal fractions less than 50%. The purple inverted triangles represent galaxies where we were only able to determine upper limits for their thermal fractions. The light blue triangles represent galaxies that were only marginally detected at 33 GHz, so no thermal fraction was calculated. At 33 GHz, the ratio of radio flux to total FIR flux is highest when $\alpha_{1.4-33}$ is flat and thermal fractions are high. These three properties are all indicative of recent star formation. Thus, it is possible that these properties together act as a rough measure of the timescale of the current episode of star formation.
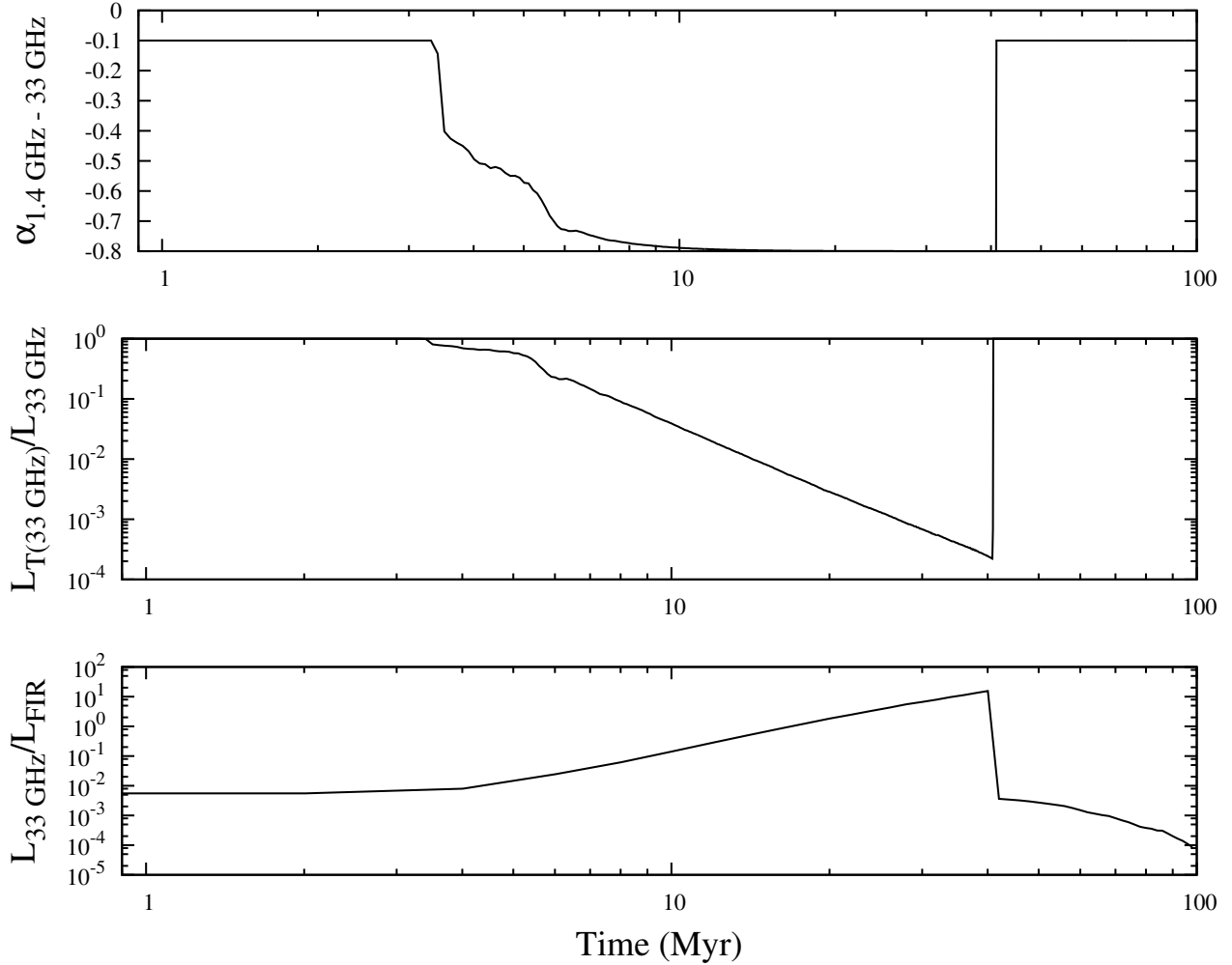
Fig. 9.—: Spectral index between 1.4 GHz and 33 GHz (top), thermal fraction (middle), and ratio of 33 GHz luminosity to total far-infrared luminosity (bottom) for a simple Starburst 99 model of an instantaneous starburst. The large jumps in each curve at 40 Myr are due to the supernova rate dropping to zero at that time, as all of the stars massive enough to produce supernovae (and thus nonthermal emission) have died. The flattest spectral indices and highest thermal fractions are seen at the earliest times after the beginning of the starburst (up to 3 Myr), while the steepest spectral indices and lowest thermal fractions are seen at later times as more supernovae occur, up to 40 Myr, after which the supernovae cease. Similarly, the higher ratios of 33 GHz luminosity to FIR luminosity were seen during the lifetimes of massive stars, while the lowest ratios of 33 GHz luminosity to FIR luminosity were seen after supernovae ended, though this trend is delayed with respect to the timelines in the top two panels. This model demonstrates that flat spectral indices, high thermal fractions, and elevated 33 GHz fluxes with respect to FIR fluxes are all indicative of very recent star formation.